②

NAVAL POSTGRADUATE SCHOOL
Monterey , California

DTIC
S ELECTE
SEP 11 1992
A D THESIS

THEORY FOR A HIGH POWER FREE ELECTRON LASER
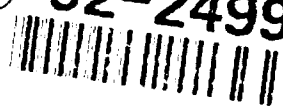AND TACTICAL APPLICATIONS

by

David J. Frost

June, 1992

Thesis Advisor: W.B. Colson

Approved for public release; distribution is unlimited

REPORT DOCUMENTATION PAGE	Form Approved OMB No 0704-0188

1a REPORT SECURITY CLASSIFICATION UNCLASSIFIED	1b RESTRICTIVE MARKINGS

2a SECURITY CLASSIFICATION AUTHORITY	3 DISTRIBUTION/AVAILABILITY OF REPORT
2b DECLASSIFICATION/DOWNGRADING SCHEDULE	Approved for public release, distribution is unlimited

4 PERFORMING ORGANIZATION REPORT NUMBER(S)	5 MONITORING ORGANIZATION REPORT NUMBER(S)

6a NAME OF PERFORMING ORGANIZATION Naval Postgraduate School	6b OFFICE SYMBOL (If applicable) 33	7a NAME OF MONITORING ORGANIZATION Naval Postgraduate School

6c ADDRESS (City, State, and ZIP Code) Monterey, CA 93943-5000	7b ADDRESS (City, State, and ZIP Code) Monterey, CA 93943-5000

8a NAME OF FUNDING/SPONSORING ORGANIZATION	8b OFFICE SYMBOL (If applicable)	9 PROCUREMENT INSTRUMENT IDENTIFICATION NUMBER

8c ADDRESS (City, State, and ZIP Code)	10 SOURCE OF FUNDING NUMBERS			
	PROGRAM ELEMENT NO	PROJECT NO	TASK NO	WORK UNIT ACCESSION NO

11 TITLE (Include Security Classification)

THEORY FOR A HIGH POWER FREE ELECTRON LASER AND TACTICAL APPLICATIONS

12 PERSONAL AUTHOR(S) Frost, David J		

13a TYPE OF REPORT Master's Thesis	13b TIME COVERED FROM ___ TO ___	14 DATE OF REPORT (Year, Month, Day) June 1992	15 PAGE COUNT 78

16 SUPPLEMENTARY NOTATION The views expressed in this thesis are those of the author and do not reflect the official policy or position of the Department of Defense or the U S Government

17 COSATI CODES			18 SUBJECT TERMS (Continue on reverse if necessary and identify by block number)
FIELD	GROUP	SUB-GROUP	Theater Ballistic Missile Defense, FEL, oscillator, amplifier, wavefront evolution, pulse evolution

19 ABSTRACT (Continue on reverse if necessary and identify by block number)

The free electron laser (FEL) shows potential as a source of coherent, high average power radiation. The achievement of high average power is one of the main topics of current FEL research. This thesis examines the Boeing Average Power Laser Experiment (APLE), whose main goal is to demonstrate the FEL's high average power capability for the first time. The experiment is in the design stage, with completion scheduled for 1996.

The first part of this thesis presents a version of a conventional Theater Ballistic Missile Defense (TBMD) system. The advantages of directed energy weapons, specifically the FEL, are also discussed.

The remainder of this thesis examines APLE. Chapter V presents research on the oscillator, and Chapter VI deals with the amplifier. Research indicates the current APLE design is feasible and can meet its design goal. Suggestions are presented for optimizing the performance of the oscillator/amplifier system.

20 DISTRIBUTION/AVAILABILITY OF ABSTRACT ☒ UNCLASSIFIED/UNLIMITED ☐ SAME AS RPT ☐ DTIC USERS	21 ABSTRACT SECURITY CLASSIFICATION Unclassified
22a NAME OF RESPONSIBLE INDIVIDUAL W B Colson	22b TELEPHONE (Include Area Code) (408) 646-2765	22c OFFICE SYMBOL PH/Cw

DD Form 1473, JUN 86 Previous editions are obsolete SECURITY CLASSIFICATION OF THIS PAGE

S/N 0102-LF-014-6603

i

Theory for a High Power Free Electron Laser
and Tactical Applications

by

David J. Frost
Lieutenant Commander, United States Navy
B.S., United States Naval Academy, 1979

Submitted in partial fulfillment of the
requirements for the degree of

MASTER OF SCIENCE IN PHYSICS

from the

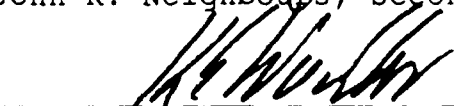NAVAL POSTGRADUATE SCHOOL
June 1992

Author: _____
David J. Frost

Approved By: _____
William B. Colson, Thesis Advisor

_____
John R. Neighbours, Second Reader

_____
Karlheinz E. Woehler, Chairman,
Department of Physics

ABSTRACT

The free electron laser (FEL) shows potential as a source of coherent, high average power radiation. The achievement of high average power is one of the main topics of current FEL research. This thesis examines the Boeing Average Power Laser Experiment (APLE), whose main goal is to demonstrate the FEL's high average power capability for the first time. The experiment is in the design stage, with completion scheduled for 1996.

The first part of this thesis presents a version of a conventional Theater Ballistic Missile Defense (TBMD) system. The advantages of directed energy weapons, specifically the FEL, are also discussed.

The remainder of this thesis examines APLE. Chapter V presents research on the oscillator, and Chapter VI deals with the amplifier. Research indicates the current APLE design is feasible and can meet its design goal. Suggestions are presented for optimizing the performance of the oscillator/amplifier system.

TABLE OF CONTENTS

ACKNOWLEDGEMENT

I. INTRODUCTION

The free electron laser (FEL) produces coherent radiation from a beam of relativistic free electrons. The principle elements of an FEL are the electron beam and a periodic magnetic field. The FEL has demonstrated the potential for high power, high efficiency, and reliability.

The FEL was first proposed by John Madey in 1970 [1]. Since that time, FELs have been operated and studied by institutions throughout the world. Possible uses include industrial, medical, scientific, and military applications. The Strategic Defense Initiative Office (SDIO) continues to study the FEL extensively for possible use as a land-based, ship-based or airborne weapon.

Chapter II addresses Theater Ballistic Missile Defense (TBMD). A version of a conventional TBMD is outlined, consisting of naval, airborne, and land-based units. The future prospects of directed energy, specifically the FEL, are also presented.

Chapter III gives an overview of FEL theory, as background for subsequent chapters. Chapter IV describes the Boeing Average Power Laser Experiment (APLE), the first FEL project with the main goal of producing high average power. APLE is in the design stage, and is scheduled to be completed in 1996.

This research will hopefully provide some additional insight into the experiment.

Chapter V presents the results of research on the proposed APLE oscillator design. Numerical simulations are used to evaluate both diffraction and pulse effects over many passes in the undulator.

Chapter VI examines both diffraction and pulse effects for the APLE amplifier. Here, a numerical simulation that evaluated pulse effects over many passes was modified to cover only one pass in the undulator.

II. THEATER BALLISTIC MISSILE DEFENSE AND THE FEL

A. BACKGROUND

Theater Ballistic Missile Defense (TBMD) is one of todays critical national defense issues [2]. The recent Gulf War underscored the importance of TBMD, both now and in the future. In the current world of only one military superpower, the United States can expect its confrontations to be largely with countries of the "third world." Many of these countries have ballistic missiles, and some are lead by despots willing to use them as weapons of terror against the United States or her allies. A workable, accurate TBMD system is crucial to U.S. interests. This chapter presents a proposed version of a system that may work in the near term. This system was first conceived and formulated while developing a project for a Combat Systems Engineering course (CC4200) at the Naval Postgraduate School. Under the guidance of Professor Mike Melich, the class studied the concept of TBMD. However, directed energy, specifically the FEL, is considered the long term solution to this difficult problem.

Modern ballistic missile warfare has its roots in the Second World War. Nazi Germany had limited success using a rudimentary ballistic missile, the V-2, to terrorize the British citizenry. The British countered ingeniously by using

deceptive radio news transmissions to draw the missiles off target.

In the recent Gulf War, the Iraqis also used ballistic missiles for terror. Iraq became aware of the acute political impact of employing ballistic missiles during its war with Iran [3]. It was to use this lesson to great effect in 1991, firing a total of 72 ballistic missiles [4]. The United States and coalition forces countered with the Patriot anti-missile system. The Patriot was originally designed for protection against manned aircraft, then updated with a limited capability against missiles. Politically, the Patriot system was a success. It helped to keep Israel out of the war, and seemed to protect the fragile coalition itself.

The military success of Patriot is now in question, however. As for the Patriot's overall track record, and for its value in theater missile defense, there seems to be little agreement. Nevertheless, experts agree that TBMD is extremely important, spurring much recent research and development. According to a Strategic Defense Initiative Organization (SDIO) official, funding for this R&D is expected to be about $500 million per year through fiscal year 1993, and to peak at about $1 billion in fiscal 1995. [5]

In the near term, the most viable candidates for active defense are the "missile-on-missile" engagement systems. However, according to Major S.A. Fleet, USAF, of the Air Command and Staff College, "one of the most difficult

challenges facing weapons designers today *is how to build a missile that is agile and accurate enough to destroy attacking warheads"* [6].

B. A NEAR TERM TBMD

The Navy can be a major player in Theater Ballistic Missile Defense. A near term TBMD system would be built around the Aegis cruiser, the Navy's most capable anti-air warfare (AAW) ship. This system would provide a mobile, quick response TBMD for the protection of U.S. interests ashore and at sea. *This recommended defense system is purely hypothetical; any association with any other conceptual systems which may or may not exist is totally coincidental.*

The heart of this TBMD system is an updated Aegis cruiser. This "update" would be a variant of the most capable Aegis phased array radar, the SPY-1D. The update would include specific hardware and software changes to tailor Aegis to the TBMD role. Battle groups will deploy with at least one of these ships. The Aegis cruiser performing this role can be called "SLINGSHOT", an acronym for **S**urface **L**aunching **S**hip on **T**heater.

Defense Support Program (DSP) satellites provide the first indication of a ballistic missile launch [5]. These satellites were originally designed to detect the relatively large plumes of intercontinental ballistic missiles. Detection algorithms and processing software in the satellites

5

ground stations were updated during the Gulf War, providing good capability against the relatively short-range theater ballistic missiles [5]. These reconnaissance satellites, with their infrared sensors, provide an initial warning and a very rough estimate of the intended target. The ground-based processing stations relay the warning to SLINGSHOT via satellite communication links.

The Aegis missile battery is the first level of defense for coastal areas. Upon receipt of a cue from the DSP satellite, SLINGSHOT will search for the missile using its special TBMD radar mode (range on the order of hundreds of miles, altitude on the order of several hundred thousand feet). After detecting the ballistic missile and establishing a firm radar "track," SLINGSHOT will engage the target with long range TBMD missiles. The Aegis system will then perform kill assessment, the results will determine whether the incoming target should be re-engaged.

For areas further inland, fighters from the battle group's aircraft carrier will be the first level of defense. The cycle of the aircraft will be like a "stack." Two pairs of F/A-18 will form an upper and lower racetrack at 35 kft and 25 kft in the vicinity of the high value area (HVA). The altitudes will largely depend on weather and aircraft loading. Meanwhile, one KA-6 will loiter in the HVA to provide fuel for the fighters. There will be another tanker (S-3 or F/A-18 with buddy stores) available between the HVA and the carrier

to act as back-up. On deck, two F/A-18 and one tanker are at alert 5 (five minute warning prior to take-off) and two F/A-18 are at alert 15. When the upper CAP's cycle is complete, they return to the carrier ("homeplate"). The lower CAP simultaneously moves to assume the upper racetrack position. The alert 5 aircraft launch and assume the lower CAP position. This "stack" continues in this manner, with the fighters low on the stack moving progressively up until they are the upper CAP. Variations of this include the CAP doing double cycles with tanking in between. This would decrease the burden on the carrier.

A broad view of a possible TBMD air engagement will illustrate this tactic. Assuming a 600 km ballistic missile flight path, one can expect a terminal speed of about 5-7 mach and a terminal angle of about 48-50 degrees (from horizontal). Positioning the CAP on the far side of the HVA provides adequate horizontal space for maneuvering into launch parameters. Upon receiving a cue from the DSP satellite, SLINGSHOT will relay the cue to the upper/lower CAP via a high speed data link. The upper CAP (loitering subsonic to conserve fuel) now turns to the target bearing, and maneuvers to meet launch parameters. These maneuvers should take several minutes. The pilot closes his firing key when he meets all parameters; SLINGSHOT can now fire the missile remotely via data link. The other upper CAP aircraft follows in trail and conducts a similar engagement, thereby increasing

the probability of kill (Pk). Immediately after the engagement, these CAP will tank with the KA-6 and then proceed to homeplate. Meanwhile, the lower CAP have moved into the upper position, and the former alert 5 aircraft are now in the lower CAP position. Aircraft control will occur via several voice communication circuits and the aforementioned data link. The carrier uses *launch and recovery* to handle the aircraft during launch and recovery operations. SLINGSHOT controls the CAP on the *war* net, while tanking is controlled by the carrier on the *admin* net. [7]

The Patriot system provides the innermost layer of ballistic missile defense. However, since Patriot is relatively immobile, it may take an additional five to ten days to be on station and operational. The Patriot battery may be "linked" with the other defense systems or it may stand alone.

The Navy does not have any anti-ballistic missiles in its current inventory. SM-2 block 4 and Erint (Extended Range Interceptor) are among the candidates for shipboard deployment. SM-2 block 4 is a future update to the Standard missile family; SM-2 block 2 is the latest available variant. Erint, a product of LTV Corporation, is designed specifically for TBMD. It is a small, agile "hit-to-kill" missile with 180 small maneuvering rocket motors [5] that supplement its fins. Erint is a good candidate for the missile to be deployed on aircraft due to its relatively small size.

C. THE MOTIVATION FOR DIRECTED ENERGY WEAPONS

The advent of gunpowder, followed by Napoleonic warfare, and Nuclear warfare were the great "watersheds" in the history of warfare [8]. It is proposed here that the use of directed energy weapons will be the next great "watershed." This natural evolution will occur because "missile-on-missile" systems have nearly reached the end of their utility.

In this section, the author makes several assumptions. The range of a surface-based directed energy weapon is assumed to be on the order of tens of kilometers; an airborne laser is assumed to have a range of hundreds of kilometers. Weather effects, which could be significant, are not considered.

The speed of modern missiles places a high premium on reaction time. An incoming Theater Ballistic Missile (TBM) with a speed of 5-7 mach (1.7-2.4 km/s) and a range of 600 km leaves about 6-8 minutes for detection and engagement. If kill assessment indicates a miss, there may be no time left for a re-engagement. The high speed of TBMs also complicate the fuzing problem in proximity warheads, requiring extremely fast fuzing and blast action. High speed targets also place additional constraints on hit-to-kill anti-ballistic missiles (ABM), requiring them to be both extremely fast and agile. The conventional ABM fly-out time must also be considered. A mach 4 ABM requires ~40 seconds to travel to a 55 km (30 NM) intercept, while a directed energy weapon requires only 0.00018 seconds. However, for a laser, dwell time on target

9

must be considered, requiring additional time on the order of a second.

Magazine depth, the amount of available ordnance, could be another critical issue. If the enemy fires a large number of TBMs during a short period of time, battle group assets could rapidly become depleted. However, some directed energy systems could conceivably have an "unlimited magazine."

In the first or second decade of the 21st century, directed energy weapons could replace the conventional TBMD weapons described in this chapter's previous section. The shipboard high energy laser (HEL) could replace the surface-to-air missile (SAM). The expected range of this HEL would be on the order of tens of kilometers. An airborne HEL, based on a relatively large airframe, would replace the TBMD fighters. The airborne laser's range would be on the order of several hundred kilometers.

Range is dependent on the level of radiation intensity on target required for a kill. This level, termed target hardness, differs with each type of missile target. According to Major Gary Danczyk, USA, of Los Alamos National Laboratory (LANL), a nominal TBM would require >1.0 kJ/cm^2 (absorbed) over a minimum axial length to ensure unstable crack propagation. Using a dwell time of 1 second, an absorbed intensity of >1.0 kW/cm^2 is required.

Range is also critically dependent on atmospheric effects. The total beam attenuation depends on the atmospheric

conditions, wavelength of the radiation, and the total atmospheric path length. Losses, particularly atmospheric scattering and absorption may be significant, raising the power requirements of the laser. Absorption can lead to an effect called "thermal blooming," a deflection and defocusing of the beam. These atmospheric effects can be minimized by using laser wavelengths that give a relatively large percent transmission. Here, a tunable laser could be advantageous. [9]

D. WHY THE FEL?

The FEL is the directed energy weapon of choice for the 21st century. It is all electric, with a potential for high efficiency, an "infinite magazine," and a continuously tunable wavelength.

VADM Kihune, USN, Vice Chief of Naval Operations for Surface Warfare, in a brief at the Naval Postgraduate School, addressed the goal of having the "all electric ship" by the year ~2015. This goal is linked directly to supporting the shipboard HEL. The FEL and the all electric ship are an excellent match because of the FEL's requirement for large electric power.

Another advantage of the FEL is its capability for relatively high efficiency. The wallplug efficiency of an FEL is the ratio of the average radiation power output to the electric power input. The single-pass extraction efficiency,

η, is the fraction of the electron beam power that is converted to optical power over a single pass. The extraction efficiency of the APLE amplifier is estimated to be ~5%. An extraction efficiency of η~40% has been demonstrated. Some FELs, such as the CEBAF experiment, estimate a wallplug efficiency as high as 40% [10].

Magazine depth is an important issue, as mentioned previously. The FEL "magazine" is likely "deeper" than that of other lasers. This is because the basis of the FEL is only electrons and a magnetic field. Other lasers use some type of active medium which would likely require periodic filtering and replenishment.

A major advantage of the FEL is its readily adjustable wavelength. Conventional lasers do not have this capability because the output wavelength is a function of the natural resonant frequency of the atom or molecule in the active medium. The FEL wavelength, λ , can be changed by changing the electron beam energy or the undulator field strength (see equation 3-8). FELs have demonstrated operation from 240 nm to 9 mm, and have exhibited continuous tunability of a single FEL over the operating wavelength by a factor of 6 [11]. This tunability would enable the FEL to take advantage of the prevailing atmospheric conditions during any TBMD engagement.

III. FREE ELECTRON LASER THEORY

A. BASIC FREE ELECTRON LASER PHYSICS

The FEL consists of two basic parts, an accelerator and an undulator or "wiggler." The accelerator produces a relativistic electron beam, while the undulator produces a periodic magnetic field (see Figure 3-1) [12]. The electron beam oscillates in the transverse direction as it moves along the undulator. The periodic, transverse acceleration of the electrons causes them to radiate in a forward cone. Some of this spontaneous radiation can be stored in a laser resonator, formed by placing two concave mirrors (one semi-transparent) at either end of the undulator. The coupling of the optical mode and the electron beam in the undulator enables kinetic energy to be extracted from the electrons. This kinetic energy is converted to electromagnetic radiation, leading to stimulated emission and coherent radiation. The FEL mechanism
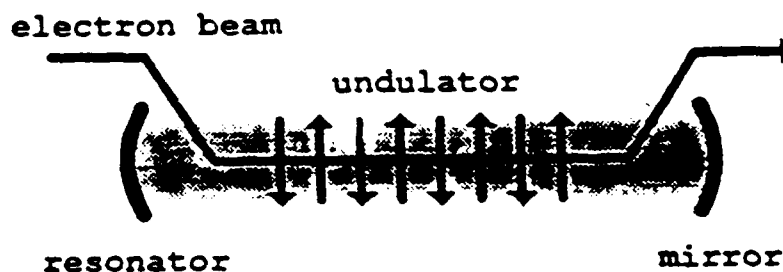

Figure 3-1. The FEL schematic.

is fundamentally classical and may be described with electromagnetic theory [13].

The accelerator provides the relativistic electron beam for use in the undulator. The beam energy, γmc^2, ranges from a few MeV to a few GeV. The Lorentz factor, $\gamma = 1/\sqrt{1-\beta^2}$, where $\beta = \vec{v}/c$ is typically in the range of $\gamma \approx 10^2$ to $\gamma \approx 10^3$. The typical FEL uses a beam energy of about 50 MeV with $\gamma \approx 10^2$. The current ranges from 1 A to 1000 A, but most FELs fall into the range from $I \approx 10$ A to 100 A. The typical power carried by the electron beam is therefore ≈ 5 GW, so that even for small efficiency the FEL can yield high peak power. However, since the electron beam from an accelerator is usually pulsed, the average power is usually much smaller.

The undulator consists of a periodic magnetic field that is either circularly or linearly polarized. The undulator length, L, can range from 1 m to more than 25 m, but is typically 5 m in length. Each undulator period, λ_0, is about 5 cm long, but can range from 1 cm to 10 cm. The resulting number of periods, N, is typically $N \approx 100$. The strength of the undulator can be described by the undulator parameter, $K = e\bar{B}\lambda_0/2\pi mc^2$, where $e = |e|$ is the charge magnitude of an electron, m is the mass of an electron, and c is the speed of light. The rms magnetic field strength, $\bar{B} = B/\sqrt{2}$ is typically a few kilogauss so that $K \approx 1$.

Figure 3-2 illustrates the interaction of an electron beam with the electromagnetic radiation within an FEL resonator. At the top frame, electrons enter the undulator where they encounter the periodic magnetic field, and begin to oscillate in the transverse direction. This oscillation causes the electrons to emit light (photons) in a forward cone. The middle frame shows a single period within the undulator. The radiation moves through one period of the undulator magnetic field as the slower electron follows a sinusoidal path. The bottom frame shows that the effect of the optical field on the electron depends on the relative phase between the electron and the optical field. Here, the electron sees the maximum radiation electric field, oriented in the same direction as the transverse motion of the electron. Since the electron is negatively charged, this field exerts a retarding force on it. The electron consequently decelerates, giving up energy to the radiation field. The energy given up by the electron is transferred to the laser beam, thereby amplifying the radiation. Energy may also be absorbed by the electron, causing it to accelerate and resulting in a loss in the optical field. Therefore, in a beam of electrons extending over many wavelengths of light, some gain energy and some lose energy. This results in "bunching" of the electron beam [14].
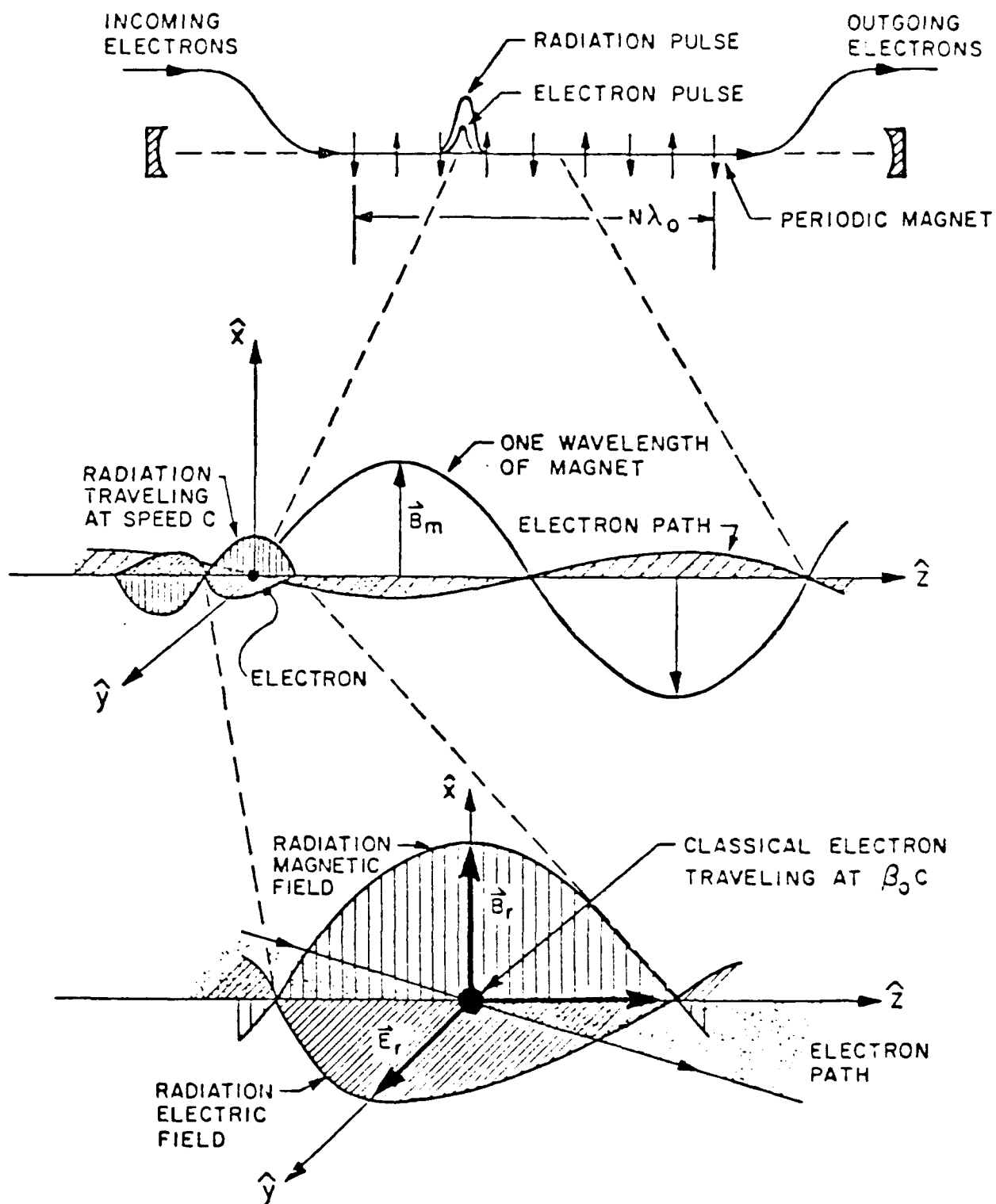
Figure 3-2. FEL optical field-electron beam interaction.

B. ELECTRON DYNAMICS AND THE PENDULUM EQUATION

The fundamental feature of the FEL is the axial bunching described in the previous section. Assuming a plane wave, the optical fields are [15]

$$\vec{E}_s = E(\cos\psi, -\sin\psi, 0), \qquad \vec{B}_s = E(\sin\psi, \cos\psi, 0), \qquad 3-1$$

where E is the optical field strength, $\psi = kz - \omega t + \phi$ with carrier frequency $\omega = kc$, $k = 2\pi/\lambda$ is the optical wavenumber correlated with the wavelength λ, and ϕ is the optical phase.

The electrons periodically deflect in the transverse direction as they travel along the undulator axis. The ideal form of the helical undulator field is

$$\vec{B} = B[\cos(k_0 z), \sin(k_0 z), 0], \qquad 3-2$$

where B is the peak undulator field strength, $k_0 = 2\pi/\lambda_0$ is the undulator wavenumber associated with the wavelength λ_0, and z is the direction along the undulator axis.

The interaction of the electrons and the optical fields inside the undulator is described by the relativistic Lorentz force [15]:

$$\frac{d}{dt}(\gamma\vec{\beta}) = -\frac{e}{mc}[\vec{E} + (\vec{\beta} \times \vec{B})], \qquad 3-3$$

and

$$\frac{d\gamma}{dt} = -\frac{e}{mc}\vec{\beta} \cdot \vec{E}. \qquad 3-4$$

Using the combined fields of the undulator and radiation, the transverse motion with perfect injection can be found to be

17

$$\beta_\perp = -\frac{K}{\gamma} [\cos(k_0 z), \sin(k_0 z), 0] + \frac{A}{\gamma} [\sin\psi, \cos\psi, 0] , \qquad 3\text{-}5$$

where $A = eE\lambda/2\pi mc^2$ is related to the optical vector potential and is analogous to the definition of K.

Using equations 3-3 and 3-4, the change of electron energy is found to be [16]

$$\dot{\gamma} = \frac{eEK}{\gamma mc} \cos(\zeta + \phi) , \qquad 3\text{-}6$$

where ζ is a dimensionless variable that describes the electron's phase with respect to the combined optical and undulator fields. Electrons with phases such that, $-\pi/2 < (\zeta + \phi) < \pi/2$, will absorb energy from the optical field causing them to accelerate. The electrons with phases, $\pi/2 < (\zeta + \phi) < 3\pi/2$, will lose energy to the optical field causing amplification. Given a random distribution of a large number of initial phases, about half the electrons gain energy and about half lose energy. However, as described earlier, under the influence of combined fields, the electrons can be made to "bunch" at desirable phases, causing gain during a pass down the undulator.

To further clarify the dynamics of electrons in the undulator, it is convenient to rewrite 3-6 in terms of ζ alone for low efficiency. Using the relation $\gamma^{-2} = 1 - \beta_\perp^2 - \beta_z^2$, and the conditions $\gamma \gg 1$, $\beta_z \approx 1$ and $\beta_\perp^2 \approx K^2/\gamma^2$, it can be shown that the

individual electrons follow motion described by the simple pendulum equation [16]

$$\overset{\circ\circ}{\zeta} = \overset{\circ}{v} = |a|\cos(\zeta+\phi) , \qquad\qquad 3\text{-}7$$

where $v = \overset{\circ}{\zeta} = L[(k+k_0)\beta_z - k]$ is the dimensionless electron phase velocity, and $|a| = 4\pi NeEKL/\gamma_0^2 mc^2$ is the dimensionless optical field strength. In 3-7, "$\circ$" means $d/d\tau$ where $\tau = ct/L$ is the dimensionless time; a pass through the undulator is described by $\tau = 0 \rightarrow 1$. The electron phase velocity, v, is a measure of the resonance between the electron beam, the undulator, and the optical field.

When $v=0$, the FEL is said to be at "resonance." The resonant wavelength is

$$\lambda = \frac{\lambda_0 (1+K^2)}{2\gamma^2} . \qquad\qquad 3\text{-}8$$

This equation shows that the operating wavelength of an FEL can be changed by changing the undulator wavelength λ_0, the undulator parameter K, or the electron beam energy γmc^2.

For high efficiency, when the change in phase velocity, v, is comparable to N, the pendulum equation can be written more accurately as

$$\overset{\circ\circ}{\zeta} = \overset{\circ}{v} = |a| (1-3v/4\pi N)\cos(\zeta+\phi) . \qquad\qquad 3\text{-}9$$

19

C. THE FEL OPTICAL WAVE EQUATION

In developing the optical wave equation it is appropriate to begin with the Maxwell's wave equation in the Coulomb gauge [15],

$$\left[\nabla^2 - \frac{1}{c^2}\frac{\partial^2}{\partial t^2}\right]\vec{A} = -\frac{4\pi}{c}\vec{J}_\perp \; , \qquad\qquad 3\text{-}10$$

where, $\nabla^2 = \partial_x^2 + \partial_y^2 + \partial_z^2$, $\vec{A} = (E/k)[\sin\psi, \cos\psi, 0]$ is the vector potential representing radiation from a helical undulator, and $\vec{J}_\perp$ is the transverse current density from the transverse motion of the electron beam. The optical field envelope is taken to vary slowly in time during an optical period ($\dot{E} \ll \omega E$, $\dot{\phi} \ll \omega\phi$), and in space over an optical wavelength ($E' \ll kE, \phi' \ll k\phi$). This is the "slow-varying amplitude and phase approximation." Using the above approximation, the left side of 3-10 can be written as

$$\left[\nabla^2 - \frac{1}{c^2}\frac{\partial^2}{\partial t^2}\right]\vec{A} \approx 2\left[\frac{\partial E}{\partial z} + \frac{1}{c}\frac{\partial E}{\partial t}\right][\cos\psi, -\sin\psi, 0] +$$

$$-2E\left[\frac{\partial\phi}{\partial z} + \frac{1}{c}\frac{\partial\phi}{\partial t}\right][\sin\psi, \cos\psi, 0] \; . \qquad 3\text{-}11$$

Replacing $\vec{J}_\perp$ with the sum of all single-particle currents, and assuming low efficiency so that the changes in γ are small even at saturation, and averaging over an optical wavelength, the wave equation may be expressed as

$$\left[\frac{\partial}{\partial z} + \frac{1}{c} \frac{\partial}{\partial t} \right] E e^{i\phi} \approx - \frac{2\pi e K \rho}{\gamma} \langle e^{-i\zeta} \rangle \; , \qquad 3\text{-}12$$

where $\zeta = (k_0 + k) z - \omega t$, ρ is the electron particle density, and $\langle \ldots \rangle$ represents the ensemble average over all the electrons. In the special case where the electron pulse is long, it has no spatial dependence. The wave equation is then independent of z and becomes

$$\overset{\circ}{a} = -j \langle e^{-i\zeta} \rangle \; , \qquad 3\text{-}13$$

where $a = |a| e^{i\phi}$ is the complex dimensionless field, and j is the dimensionless current density :

$$a \approx \frac{4\pi N e K L E e^{i\phi}}{\gamma^2 m c^2} \; , \qquad j = \frac{8N(e\pi KL)^2 \rho}{\gamma^3 m c^2} \; . \qquad 3\text{-}14$$

For a linear undulator the derivation is similar, except that K is replaced by $K(J_0(\xi) - J_1(\xi))$, where $\xi = K^2/2(1+K^2)$. The Bessel function factor accounts for reduced coupling in the linear undulator due to fast periodic z motion of the electrons [17].

For the high efficiency case when the changes in v can be as large as N, the wave equation can be more accurately written as

$$\overset{\circ}{a} = j \langle (1 - v/4\pi N) \, e^{-i\zeta} \rangle \; . \qquad 3\text{-}15$$

D. FEL DIMENSIONLESS PARAMETERS

A few dimensionless variables can summarize recurring combinations of physical parameters in a complex problem like the FEL. Several dimensionless variables are used to gain insight into relevant physical processes without detailed calculations or simulations [12].

Some dimensionless variables have already been introduced. The undulator parameter, K, is an important quantity characterizing many FEL properties such as the electron deflection angles. The electron phase and phase velocity, ζ and ν, define bunching of electrons and their bunching rate. The optical field strength $|a|$, can also be used as an indicator of expected electron bunching rate since $\overset{\circ}{\nu} \propto |a|$.

The dimensionless current density j (see 3-14) determines the response of the optical field to electron beam bunching. It also provides the coupling between the electron beam and the light wave. The FEL's gain regime is determined by the value of j: when $j \sim 1$, or less, the FEL gain is low, and when $j \gg 1$ the FEL gain is high.

The slippage distance, $N\lambda$, is used to normalize longitudinal distances in the FEL. The slippage distance is the distance that light passes over an electron as the electron travels through the undulator. It is the characteristic distance in the trapped-particle instability and short-pulse evolution. At resonance, exactly one

wavelength of light passes over an electron as the electron travels through an undulator wavelength.

The characteristic optical beam radius, $(L\lambda/\pi)^{1/2}$, normalizes transverse dimensions in the FEL. This is done by multiplying the dimension, such as the electron beam radius, by $(\pi/L\lambda)^{1/2}$.

The "filling factor", F, is the ratio of the electron beam area to the optical mode area, averaged over the undulator length, and determines the effect of transverse optical mode distortion.

E. THE HIGH GAIN REGIME

When the dimensionless current density is large enough so that $j \gg 1$, the optical wave amplitude and phase change significantly during the FEL interaction, usually resulting in high gain. Maximizing j with the aim of achieving high gain depends on several factors. At short wavelengths, j tends to be relatively small because more relativistic electrons are difficult to bunch (refer to equations 3-8 and 3-14). Working at longer wavelengths will increase j, but the optical wavelength is usually determined by the laser's application. The length of the undulator, L, can also be increased, but this increases the FEL's sensitivity to beam quality. On the other hand, when the current increases markedly, the beam quality from the accelerator starts to decrease. In other words, the penalty for achieving a large j is often a

23

corresponding decrease in beam quality leading to poor gain. However, this degradation can be offset by mode distortion (see section III.I.).

The wave and pendulum equations are valid in the high gain regime, and can be solved numerically to explore phase space evolution. In weak optical fields, the equations can also be solved analytically. Expanding the pendulum and wave equations, and integrating over all initial phases $\int d\zeta_0$, we can obtain an integro-differential equation governing the evolution of the optical field [18],

$$\overset{\circ}{a}(\tau) = \frac{ij}{2} \int_0^\tau d\tau' \tau' F(\tau') e^{-iv_0\tau'} a(\tau-\tau') \ , \qquad 3\text{-}16$$

where $F(\tau') = \int dq\, f(q)\, e^{-iq\tau'}$ is the characteristic function of the distribution $f(q)$, $f(q)$ is the distribution of initial electron phase velocities $v_1 = v_0 + q$ about v_0, and $\int dq\, f(q) = 1$.

The integral equation 3-16 is valid for both high and low current. The equation can be solved analytically or numerically. In the limit of weak optical fields, the integral equation has an advantage over a simulation that must follow the evolution of many sample electrons. In the high current limit $j \gg 1$, the integral equation can be solved

24

analytically to obtain the gain for a perfect beam [12],

$$G(\tau) \approx \frac{1}{9} e^{(j/2)^{1/3}\sqrt{3}\tau} \ . \hspace{2cm} 3\text{-}17$$

At high current, inter-electron Coulomb forces may effect electron bunching. These forces are negligible except for a value of j that would result in extremely high gain; in this case, the high gain itself would already cause much more dramatic collective effects. Coulomb forces can also cause distortion of the electron pulse, but this is usually an insignificant effect [12].

F. THE TAPERED UNDULATOR AND HIGH EFFICIENCY

High efficiency is usually desirable in the FEL. A tapered undulator is required in order to achieve high extraction efficiency, η, the fraction of electron beam energy converted to light. The maximum extraction efficiency of an untapered undulator is $\eta \approx 1/N$ and is typically only a few percent [19]. In a tapered undulator, about 50% of the electrons are coherently decelerated in ponderomotive potential wells, or "buckets," formed by the combined undulator and radiation fields. These "trapped" electrons continue to lose energy to the light wave as the undulator length is increased, so that η may exceed $\approx 1/N$.

The beginning section of the undulator should be untapered with a constant peak magnetic field B and spatial period λ_0. This allows the power in the light wave to grow to saturation

where trapping begins. After saturation without taper, the laser power will decrease with undulator length as electrons absorb power from the light. Equation 3-8 shows that as the electron energy γ decreases at saturation, either λ_0 or K can be changed to compensate, maintaining the resonant wavelength through the undulator. The basic idea of tapering is to change the undulator parameters, B or λ_0, to maintain resonance with the radiation field as the trapped electrons lose energy.

Decreasing the undulator field strength, or the undulator wavelength, results in a phase acceleration, $\ddot{\zeta} = \delta + \ldots$ where $\delta = 8\pi N \eta_{desired}$ and $\eta_{desired}$ is the desired efficiency assuming 50% of the electrons are trapped. When $N \gg 1$, the phase acceleration can be significant with only a small change in the undulator properties.

Recall that the pendulum and wave equations, 3-9 and 3-15, had a correction factor for high efficiency. For a high efficiency, tapered undulator $\dot{v} = \delta$, and $\Delta v \approx \delta \Delta \tau \approx \delta$ for $\Delta \tau = 1$. Using the identity in the previous paragraph with a desired efficiency of 5%, yields $\delta = 4\pi N/10$. Taking $\langle \Delta v \rangle \approx 4\pi N/10$ and the fact that $v \rightarrow \Delta v$, results in correction factors of $1 - 3\langle v \rangle / 4\pi N \approx 0.7$ and $1 - \langle v \rangle / 4\pi N \approx 0.9$ in 3-9 and 3-15, respectively. On the other hand, $\Delta v \approx \pi$ for the untapered undulator, resulting in the correction being ≈ 1 and therefore not used.

26

G. SHORT OPTICAL PULSES

Short, picosecond long electron pulses from an RF accelerator drive many FEL oscillators and some FEL amplifiers. When the electron pulse length is comparable to the slippage distance $N\lambda$, short-pulses will effect the FEL interaction [20-25]. If the electron pulse length is much longer than the slippage distance, the pulse is considered long. The performance of the APLE oscillator is somewhat independent of the short optical pulse effects, but the pulse effects that do occur will effect the amplifier.

Within the FEL oscillator short electron pulses lead to short optical pulses via spontaneous emission. This light bounces inside the resonator between concave mirrors separated by a distance S. The electron pulses from the accelerator must be synchronized to arrive at the beginning of the undulator, $\tau=0$, coincident with the rebounding light. The distance between the electron and the optical pulse at $\tau=0$ is termed "desynchronism," $d=-\Delta S/N\lambda$, and is normalized to the slippage distance. When $d=0$, there is exact synchronism between the light and the electron pulse.

Recall that on each pass down the undulator, the unbunched electron pulse starts at $\tau=0$ and slips back with respect to the light as bunching develops. The bunched electron pulse tends to drive the trailing edge of the light pulse, distorting it on each pass. As a result, the centroid of the light pulse slows to below c. To compensate for the slower

speed of the light pulse, the path S must be reduced so that $d \approx 0.001 \rightarrow 0.1$ [12]. In practice, moving one of the resonator mirrors a small distance ΔS adjusts the value of d. The adjustment must be chosen carefully since the incorrect value of d will adversely effect the overlap of the electron beam and the optical mode, thereby reducing gain.

The general features of short-pulse behavior have been observed in many simulations and several experiments [12]. At small desynchronism, $d \sim 0$ or greater, the power is often large enough to cause the trapped-particle instability, a broad optical spectrum, and a broad electron spectrum. The optical pulse is short and is centered on the electron pulse. The FEL tends to be unstable at small values of desynchronism, since a small change in d can make a large difference in steady-state power.

For larger d, the FEL becomes more stable. At large desynchronism, the steady-state power is smaller due to the reduced coupling, and the trapped-particle instability usually does not occur. The final optical pulse can be much longer than the electron pulse, resulting in a narrow power spectrum. The electron spectrum is narrow in the weaker optical fields, and the center of the optical pulse may actually be well ahead of the electron pulse. The FEL's operating range in d is typically $\Delta d \approx 0.1$, so that the resonator length must be adjusted within a surprisingly small range $\Delta S \approx -5$ μm for $N = 10^2$ and $\lambda = 1 \mu$m.

28

H. THE FEL TRAPPED-PARTICLE INSTABILITY

When either the FEL amplifier or oscillator reaches power levels beyond the onset of saturation, the FEL may experience the trapped-particle instability. Electrons can become trapped in deep potential wells in phase space when under the influence of strong optical fields $|a| >> \pi$. The oscillation of the beam current that is trapped in these wells can drive the carrier wave unstable, causing sideband frequencies to grow from noise. The trapped-particle instability can then modify or destroy the coherence that is initially established in weak optical fields. This instability can be exhibited in a wide range of undulator designs operating in strong fields [26-31].

The general features of the trapped-particle instability in the FEL oscillator depend only on the dimensionless current j and the loss factor Q. For sufficiently low values of j and Q, the trapped-particle instability does not occur; however, increasing either j or Q can result in the instability.

The trapped-particle instability in an FEL is a mixed blessing. A high-power laser with a narrow spectrum and no sidebands is often desirable to the experimenter. However, the presence of sidebands indicates the achievement of high power and that the FEL is operating well. In fact, the FEL attains even higher power and efficiency as more sidebands develop. High power tends to result in both a broad electron spectrum and a broad optical spectrum, but tapering tends to diminish the instability.

29

In the amplifier, the electron beam interacts with the optical field for only one pass. Therefore, only the largest values of $j \approx 10^5$ have a possibility of developing a significant sideband. Because of this requirement, the trapped-particle instability has never been observed in the FEL amplifier.

I. FEL MODE DISTORTION

The FEL interaction modifies both the optical phase and the wavefront. When considering transverse effects, the optical field is given transverse spatial dependence, $a(x,y,t)$. In this case, the parabolic wave equation is

$$\left[-\frac{i}{4} \nabla_\perp^2 + \frac{\partial}{\partial t} \right] (x,y,\tau) = -\langle j e^{-i\zeta} \rangle_{(x,y,\tau)} , \qquad 3\text{-}18$$

where $\nabla_\perp^2 = \partial_x^2 + \partial_y^2$ must be used to include the effects of

diffraction [12]. In either strong or weak fields, the FEL interaction causes a phase shift that is opposite to that of natural diffraction, and therefore focusses the light back into the electron beam along z. For large current j and a small electron beam, this focussing can decrease the transverse area of the optical mode, thereby increasing the effective F. The net result is an increase in the effective dimensionless current, jF, leading to higher gain.

J. BEAM QUALITY

Recall that optimizing an FEL experiment often leads to a design trade-off between high beam current and poor beam quality as defined by the accelerator. A given application usually fixes the optical wavelength λ so that the dimensionless current, $j \propto I N^3 \lambda^{1/2}$, must be maximized with the current I and the number of undulator periods N. However, increasing I tends to decrease beam quality from the accelerator, while increasing N increases the FEL's sensitivity to beam quality because the gain bandwidth is narrower. The consequence of poor beam quality is a reduction in FEL performance due to degraded bunching [12].

Beam quality is generally described by two qualities: the beam energy spread, $\Delta\gamma/\gamma$, and the beam emittance, ε. The energy spread is a measure of the spread in electron velocity magnitudes. The Gaussian distribution of energies with rms spread, $\Delta\gamma/\gamma$, can be characterized by $\sigma_G = 4\pi N \Delta\gamma/\gamma$; when $\sigma_G \approx \pi$ bunching is impaired. The value of σ_G gives the spread in electron phase velocities $\Delta\nu$ in the beam. Emittance is a measure of the spread in electron velocity directions or angles.

Emittance is given by $\varepsilon = \bar{r}\bar{\theta}$ where $\bar{r}$ is the average beam radius, and $\bar{\theta}$ is the average beam angular divergence. When the beam is focused to a small radius $\bar{r}$, the angular spread $\bar{\theta}$ increases keeping the emittance ε fixed. As the beam is accelerated, and the beam energy γmc^2 is increased

31

significantly, the normalized emittance $\varepsilon_n = \gamma\varepsilon = \gamma\bar{r}\bar{\theta}$ tends to remain constant and is a useful measure of beam quality. A Gaussian spread in angles with rms value $\bar{\theta}$, results in an exponential distribution of phase velocities with characteristic width $\sigma_\theta = 4\pi N\gamma^2\bar{\theta}^2/(1+K^2)$. When σ_θ is equal to or larger than π, electron bunching is impaired.

IV. THE AVERAGE POWER LASER EXPERIMENT

The Average Power Laser Experiment (APLE) is one of the most significant studies in the free electron laser field. Although the FEL has potential for use in a wide range of disciplines, it currently has been designed for only mediocre average power. This experiment, now under development, intends to demonstrate the high-average power capability for the first time.

APLE [32] is a cooperative effort between Boeing Corporation and the Los Alamos National Laboratory (LANL). Its objective is to design, construct, and demonstrate an integrated, high duty factor, 10 micron wavelength free electron laser by 1996. The primary design goal is to sustain 100 kW average power for at least three minutes. The design parameters are listed in Table 4-1 [33]. The device will operate in the single accelerator, master-oscillator, power amplifier (SAMOPA) mode, with the oscillator providing a seed laser of about 100 watts to drive the amplifier. In the acronym SAMOPA, "SA" refers to the APLE accelerator that powers both the oscillator and amplifier; "MO" refers to the FEL oscillator, and "PA" refers to the FEL amplifier. The cost of APLE is approximately 100 million dollars; initially

TABLE 4-1.   APLE FEL DESIGN PARAMETERS.

Configuration	- Single accelerator oscillator amplifier	
	Laser power - 100 kW	
	Wavelength - 10.6 μm	
	Run time - 3 minutes	
Electron beam	Oscillator	Amplifier
Energy	17 MeV	34 MeV
Avg. current (macro)	0.23 A	0.23 A
Avg. power (25% duty)	1 MW	2 MW
Pulse length (macro)	10 ms	10 ms
Pulse rate (micro)	27 MHz	27 MHz
Pulse length (micro)	60 ps	18 ps
Peak current	140 A	450 A
Normalized emittance	80π (mm-mrad)	80π (mm-mrad)
Energy spread (micro)	0.3%	0.75%
Laser		
Extraction efficiency	0.01%	5%
Laser power	100 W	100 kW
Resonator	22 m concentric	--
Wiggler length	2.36 m	9.96 m
Wiggler period	2.36 cm	3.89 cm

34

the end date was set at 1994, but the project will run longer due to funding limitations [34].

The existing Boeing FEL facility in Seattle, Washington, is the sight of the experiment. The laboratory complex provides virtually all the required housekeeping support. A visit to Boeing in November 1991 revealed a large two story building with a basically empty second floor; this area will eventually house the laser. The amplifier wiggler and many crates of support equipment are on location. Much of the hardware and software to be used on APLE are on site because of use on previous FEL experiments.

The main components of APLE are shown in Figure 4-1 [32]. They are the photoelectric injector, the accelerator, the oscillator and amplifier wigglers, the beam transport optics, and the electron beam dump. The accelerator is separated into two sections by the oscillator wiggler and associated hardware. Each accelerator section is powered by two klystrons.

A general system description starts with the production of electron micropulses in the photoelectric injector. The electrons exiting the injector have a normalized emittance (90% edge) of 80π mm-mrad. These electrons are then accelerated to 17 MeV at a current of 0.23 A by the first section of the accelerator. At the end of the first accelerator section, the beam is focused, bent, then re-focused prior to entrance into the oscillator wiggler. The
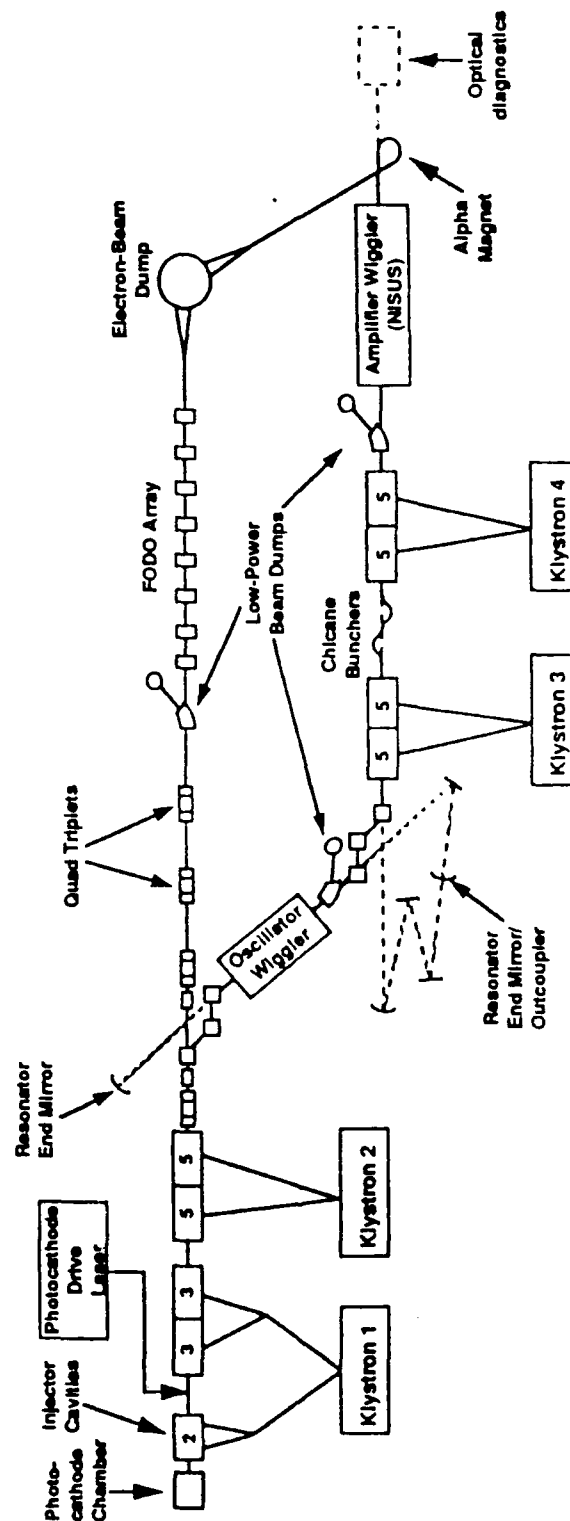
Figure 4-1.   The APLE layout.

electron beam exiting the oscillator wiggler is then bent into the second section of the accelerator. The energy spread (90% edge) in the wiggler is 0.3%. Two interleaved chicane bunchers separate this section into two segments. The first segment boosts the electron energy to 25.5 MeV and is phased to impart a 2.6% energy slew on the electron pulses. This slew is necessary in order to bunch the beam in the subsequent chicane bunchers, which compress the beam micropulses from 60 ps to 18 ps FWHM. The reduction of the electron micropulse length from 1.8 cm to 0.54 cm increases the peak current in order to increase the amplifier gain. The final accelerator segment increases the energy to 34 MeV at a current of 0.23 A and removes the energy slew from the beam before it enters the amplifier wiggler. The energy spread in the wiggler is 0.75%. After exiting the amplifier wiggler, a magnet directs the beam into the main beam dump. The built-in flexibility of the APLE layout allows the electron beam to travel straight-ahead, through the oscillator wiggler only, or through both the oscillator and amplifier wigglers. Preconditioning of the beam prior to injection into the wigglers is possible via the straight-ahead path (upper path on Figure 4-1). The low power beam dumps will permit early tuning of the oscillator accelerator, both during APLE construction and afterward when in operation.

The amplified light is produced via the systems two undulators. The oscillator wiggler will be designed by STI

Optronics, Inc. [32]. It has a period λ_b=2.36 cm and a length L=2.36 m, thereby consisting of N=100 periods. The mirror separation distance, S, is 22 m. The APLE oscillator is designed to produce a relatively low-power seed laser beam, typically 100 watts. This power can be easily found by taking the oscillator potential of 17 MV with the current of 0.23 A to get a power of 1 MW (at 25% duty). The extraction efficiency of 0.01% yields the laser power of 100 W. This laser beam passes through the amplifier concurrently with the electron beam to produce the 100 kW laser beam. The seed laser pulses produced by the oscillator are directed to the amplifier wiggler by a series of optics.

The amplifier wiggler is L=9.96 m long, and consists of N=256 periods which are each λ_b=3.89 cm in length; design extraction efficiency is 5%. Both wigglers have a tapering capability. The optical beam pulses must properly overlap the electron beam pulses to maintain coupling in the amplifier section [12]. The required overlap of the short electron and optical pulses is achieved by control of the path length and direction of the optical beam using adjustable mirror mounts, two in the resonator and one in the beam train between the oscillator and the amplifier. The laser beam then propagates from the amplifier in a 27 m long vacuum pipe to an optical diagnostic area [32].

Heating of the oscillator mirrors can be a problem; therefore, it is important to know the laser beam intensity on

the mirror surface. A critical motivation for using the MOPA configuration is to circumvent mirror heating problems through use of the high-gain amplifier, which has no mirrors. The first step is to solve for the laser spot size at the resonator mirror, $w^2 = w_0^2 (1 + z^2/z_0^2)$, where w is the spot radius at position z, z is the distance to the mirror from the mode waist, and z_0 is the Rayleigh range. The Rayleigh range is defined as $z_0 = \pi w_0^2/\lambda$, and is $z_0 = L/2 = 118$ cm for the oscillator resonator. Then, the spot area on the mirror is 11.2 cm^2. With a laser power of 100 W, the intensity is 8.9 W/cm^2 deposited on the mirrors. This intensity is quite modest and will not cause any heating problems.

One of the major improvements of APLE over Boeing's previous experiments should be improved beam quality [34]. The successful operation of any FEL is critically dependent upon the quality of the electron beam. As discussed in the previous chapter, beam quality is generally described by two quantities: the beam energy spread, $\Delta\gamma/\gamma$, and the beam emittance, ε. The beam emittance, ε, is established by the injector [35]. The high beam quality must be maintained as the beam is accelerated and transported to the wiggler. Boeing's previous FEL [36] exhibited the following. $\Delta\gamma/\gamma = .005$ (FWHM) at 250 Amps, and $\varepsilon_n = \gamma\varepsilon \approx 100\text{-}120\pi$ mm-mrad. The design values for APLE are: $\Delta\gamma/\gamma = .004$ (FWHM) at 450 Amps, and $\varepsilon_n \approx 40\pi$ mm-mrad (FWHM). In order to maximize beam quality, Boeing

39

chose the photoelectric cathode injector over the thermionic gun. APLE will be the first to use a laser-driven, photocathode injector in high-duty operation [32].

Recall that a few dimensionless variables can summarize recurring physical properties in the FEL. Table 4-2 shows some of the important FEL dimensionless parameters.

TABLE 4-2. APLE DIMENSIONLESS PARAMETERS.

Parameter	Oscillator	Amplifier
j, current density	250	197000
K, undulator parameter	0.23	1.22
N, number of periods	100	256
F, filling factor weak fields, single-mode	0.12	0.0094
F, filling factor strong fields, multi-mode	0.04	0.10
σ_G, gaussian distribution energy spread	1.0	6.0
σ_θ, exponential distribution energy spread	1.5	7.0

V. THE APLE OSCILLATOR

A. DIFFRACTION EFFECTS

In this chapter, numerical simulations are used to investigate important features of the APLE oscillator. These simulations use the parabolic wave equation [12] to solve for the natural diffraction and transverse mode distortion in the optical wavefront. Only one field site in the longitudinal dimension is followed, but the simulation output includes evaluation of the FEL efficiency, gain, and the transverse optical mode - electron interaction.

One of the initial steps in the investigation is to find the initial FEL phase velocity, v_0, for maximum gain. The initial phase velocity determines the FEL gain at the end of the undulator [12]. A gain spectrum is obtained by calculating the gain as a function of phase velocity. The peak gain is then selected directly from the gain spectrum, and the corresponding value of v_0 is used in subsequent numerical simulations.

The APLE dimensionless parameters are used as inputs to the numerical solution of the gain spectrum. The dimensionless current density is $j=250$, and the radius of the electron beam is $\sigma_e = r_e(\pi/L\ \lambda)^{1/2} = 0.28$. The beam quality is accounted for by using the distributions $\sigma_\theta = 1.5$ and $\sigma_G = 1.0$. The dimensionless Rayleigh length, $z_0 = Z_0/L = 0.5$, is found by

41

dividing the dimensional Rayleigh length by the undulator length L. The position of the optical mode waist along the undulator is described by $\tau_w=0.5$ when centered at the middle of the undulator at $L/2$. The initial dimensionless optical field strength is estimated as $a_0=0.01$ in the weak field regime. The electron beam traverses through $N=100$ periods during a single trip through the undulator.

Figure 5-1 shows the spectrum of final gains, $G(\nu_0)$, plotted against the initial phase velocity ν_0. The peak gain of $G{\approx}23.5$ occurs at $\nu_0{\approx}5$, and the spectrum is nearly symmetric
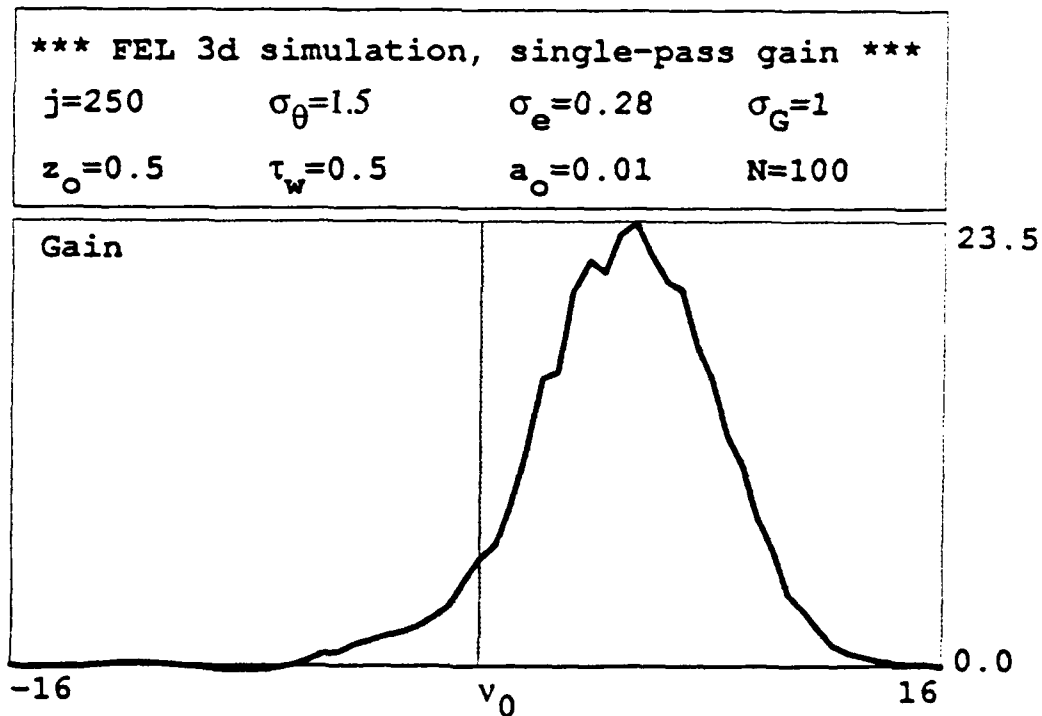
Figure 5-1. Gain spectrum of the APLE oscillator.

about $v_0 \approx 5$. If the gain bandwidth is defined by the range of phase velocities over which the gain is reduced by $\approx 1/e$, then $\Delta v_0 \approx 2\pi$. When natural diffraction is included, the optical phase changes according to $\phi(\tau) \approx -\tau/z_0 \approx -2\tau$ along the undulator, and gives a shift in resonance by $\Delta v_0 \approx 1/z_0 \approx 2$ [12]. The energy spread shifts the gain spectrum to higher values of v_0 so that the peak gain should occur close to $v_0 \approx 5$ as is seen. The gain spectrum shows how the gain changes when the optical wavelength varies through $\Delta v_0 \approx 2\pi N \Delta \lambda / \lambda$ around the resonant wavelength, or when the electron beam energy varies through $\Delta v_0 \approx 4\pi N \Delta \gamma / \gamma$ around the resonant energy.

The FEL wavefront evolution as τ goes from 0 to 1 along the $N=100$ period undulator is illustrated in Figure 5-2 via the results of a numerical simulation. The input parameters are similar to those in the gain spectrum simulation. The effects of both energy spread (σ_G) and emittance (σ_θ) are accounted for, and we use the additional parameter $v_0 \approx 5$.

The evolution of the optical mode amplitude, $|a(x,\tau)|$ (upper-left), is shown as an intensity/contour plot. The maximum field is black and the zero field is white; the white contour line represents the field at 50% of the maximum amplitude shown on the right. The grey scale associated with these plots is shown in the upper-right window. The evolution shows that the peak field, in the center of the optical mode, grows steadily through the undulator. The upper-center frame shows the mode, $|a(x,y)|$, at the end of the undulator; x and

43

y axes are normalized by $(L\lambda/\pi)^{1/2}$, where $L=236$ cm and $\lambda=10.6$

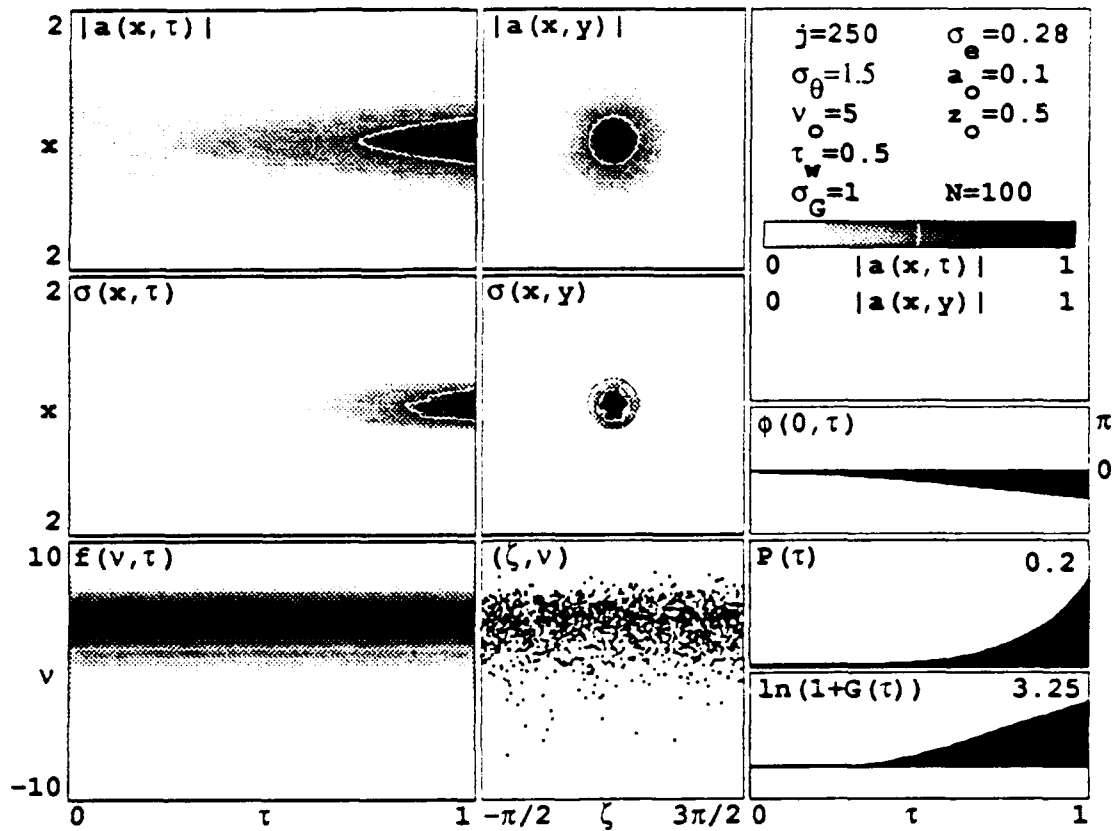μm. The evolution of the bunching current, $\sigma(x,\tau)$ (middle-

Figure 5-2. Numerical simulation of the APLE oscillator wavefronts in weak fields.

left), shows the amount of bunching in the electron beam along the length of the undulator. There is no bunching at the beginning of the undulator ($\tau=0$), but there is clear bunching at the end of the undulator ($\tau=1$). The middle-center frame shows the electron bunching at the end of the undulator $\sigma(x,y)$. Recall that the filling factor, F, is the ratio of the electron beam area, $\approx \pi(\sigma_e)^2$ where $\sigma_e=0.28$, to that of the optical mode. The focussing of the optical mode increases the

44

value of F, and serves to increase the gain. The electron phase velocity distribution, $f(v,\tau)$ (lower-left), shows negligible distortion of the electron beam in the weak optical field. The final electron phase-space distribution, (ζ,v) (lower-center), shows a small amount of electron bunching at the end of the undulator. The spread in phase velocities due to the initial spread $\sigma_G \approx 1$ and $\sigma_\theta \approx 1.5$ is clearly visible. The plot of the optical field phase evolution at the center of the mode, $\phi(0,\tau)$ (on the right), indicates an almost linear decrease in phase. This is caused by natural diffraction giving a phase shift of $\phi(\tau) \approx -\tau/z_0 \approx -2\tau$ over the length of the undulator. The power evolution, $P(\tau)$, shows a progressive increase in power as bunching develops. The gain, $G(\tau)$, also increases with the increased bunching of electrons; the final gain is $G_f \approx 25$.

Figure 5-3 gives the result of a simulation with nearly no current ($j=0.001$) in order to show the laser mode, $|a(x,y)|$, at the end of the undulator due to natural diffraction. The wavefront is initialized to have Rayleigh length $z_0=0.5$ centered in the middle of the undulator at $\tau_w=0.5$. The mode waist radius is $w_0=(z_0)^{1/2} \approx 0.707$. At the beginning and end of the undulator, the mode radius is given by $w = w_0 (1 + 0.5^2/z_0^2)^{1/2} \approx \sqrt{2} w_0 \approx 1$ as is seen in the figure. The mode in figure 5-2 is clearly smaller with a radius of $w \approx 0.4$, as the high current electron beam has focussed the light inward toward the beam.
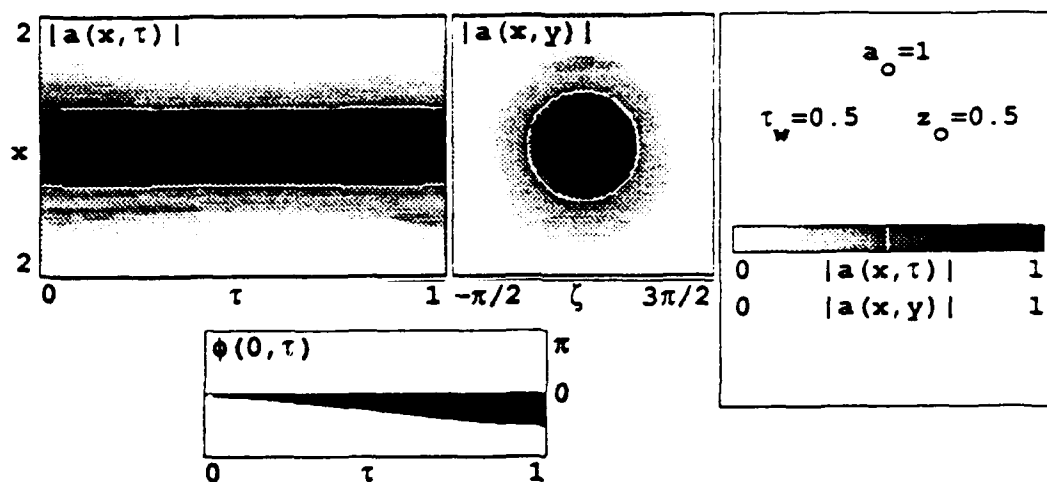
45

Figure 5-3. Optical mode at the end of the undulator, when only governed by diffraction.

Figure 5-4 is another numerical simulation of the FEL wavefronts, but with a different input parameter. The
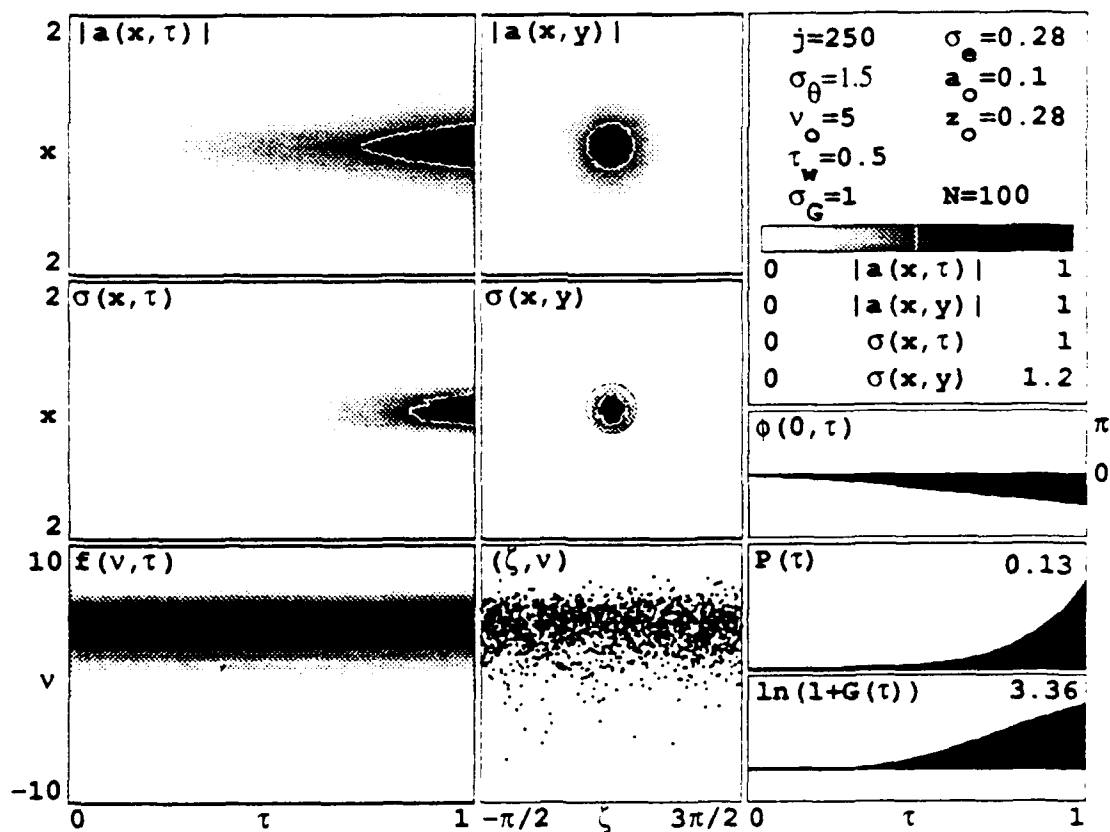

Figure 5-4. APLE oscillator wavefronts with an exponential energy spread, and a $z_0=0.28$.

Rayleigh length $z_0=(1/12)^{1/2}=0.28$ vice $z_0=0.5$. The smaller Rayleigh length of $z_0=(1/12)^{1/2}$ focusses the optical wavefront around the electron more tightly all along the undulator, and increases coupling. The overall result is a significantly higher final gain of $G_f\approx28$.

We now investigate the oscillator wavefronts through successive passes of the undulator. This numerical simulation includes inputs similar to those in Figure 5-2, with some added parameters. The FEL system simulated now includes mirrors. The dimensionless mirror radius $r_m=2.4$ is normalized by $(L\lambda/\pi)^{1/2}$. The dimensionless radius of curvature of the mirror $r_c=1.2$ is normalized by L. Figure 5-5 shows the results of this simulation for $n=32$ passes through the undulator. The mirror surface near the beginning of the undulator is taken to be perfectly reflecting. The mirror surface near the end of the undulator is given a loss described by $Q=5$, defined so that over many passes n, the power loss would be given by $\propto e^{-n/Q}$. Each mirror radius is determined so that 1% of the optical power in the fundamental mode goes around the mirror, as indicated by edge loss. The radius of curvature of each mirror is determined by the Rayleigh length of the optical mode, $z_0=0.5$, and the position of the mode waist, $\tau_w=0.5$. The distance between the mirrors is taken to be twice the undulator length with the undulator centered between the mirrors. This resonator length is much less than anticipated in the experiment, but allows a

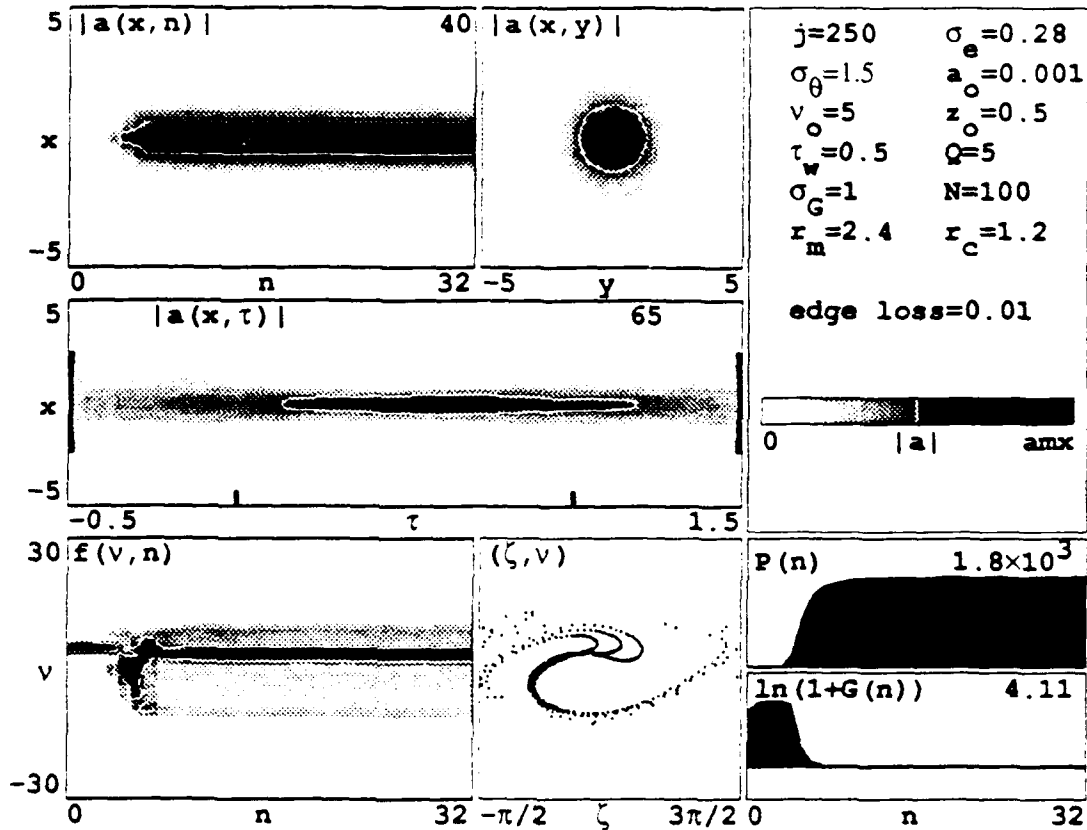numerical solution and represents the appropriate Rayleigh
length.

Figure 5-5.   APLE oscillator wavefront evolution over n=100
passes.

The evolution of the optical mode amplitude (upper-left),
shows that the field amplitude grows with each successive pass
down the undulator until reaching a maximum amplitude of
$|a(x,n)|$=40.   The upper-center frame is an "end-on" view of
the optical mode at the end of the undulator on the final
pass.   The middle window depicts the optical field amplitude,
$|a(x,\tau)|$, along the length of the resonator from mirror to
mirror on the final pass.   Notice that the largest field

48

amplitude is near the center of the undulator at the focus of the mode waist near $\tau_w=0.5$. The lower-left window shows the evolution of the electron phase velocity distribution, $f(v,n)$, over successive passes. The electron phase-space evolution (ζ,v) at the end of the final pass (lower-center), shows significant electron bunching in closed phase-space paths and strong optical fields. The power evolution with each pass, $P(n)$, shows a steady increase in power followed by relatively steady power at saturation. This is also reflected in the plot of gain (lower-right), $G(n)$.

B. PULSE EFFECTS

In this section, we use numerical simulations to investigate the multimode pulse effects of the APLE oscillator. We begin by observing the electron phase-space evolution, and then investigate the FEL pulse evolution.

Figure 5-6 shows the result of solving the pendulum and wave equations numerically with 2000 sample electrons in a strong optical field $a_0=4\pi^2\approx40$ and for low current of $jF=10$ where $j=250$ and estimating $F=0.04$. The electrons are started with a random Gaussian spread corresponding to $\sigma_G=1$ and emittance corresponding to $\sigma_\theta=1.5$ about the phase velocity $v_0=5$. The final phase-space positions of the electrons are drawn in (ζ,v). The final positions of the electrons show overbunching, with many electrons trapped in the closed orbits of phase-space. Some of the electrons show an increase in

49

energy, or phase velocity v. These electrons absorbed energy
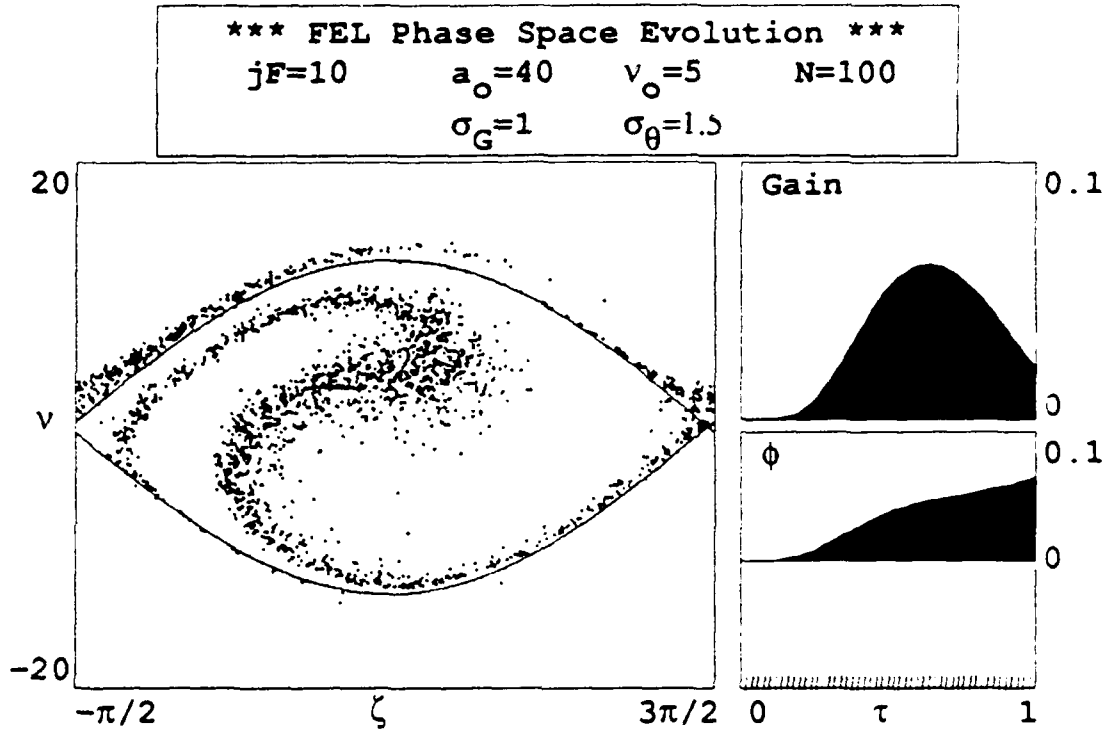from the optical mode, resulting in a decrease in gain at the

Figure 5-6. APLE oscillator strong-field phase-space
evolution with low current.

end of the undulator. This decrease is evident in the
corresponding curve to the right.

Figure 5-7 shows the APLE oscillator pulse evolution over
n=800 passes with no initial field ($a_0=0$), starting at
resonance $v_0=0$. The window width w=30 corresponds to thirty
slippage distances along the beam, z is the longitudinal axis.
The dimensionless current density is $jF=10$. The dimensional
electron pulse length is normalized by $N\lambda$ to get the
dimensionless electron pulse length, $\sigma_z=17$ (FWHM). The

50

desynchronism (see section III. G.), defined by $d=0.0001$,
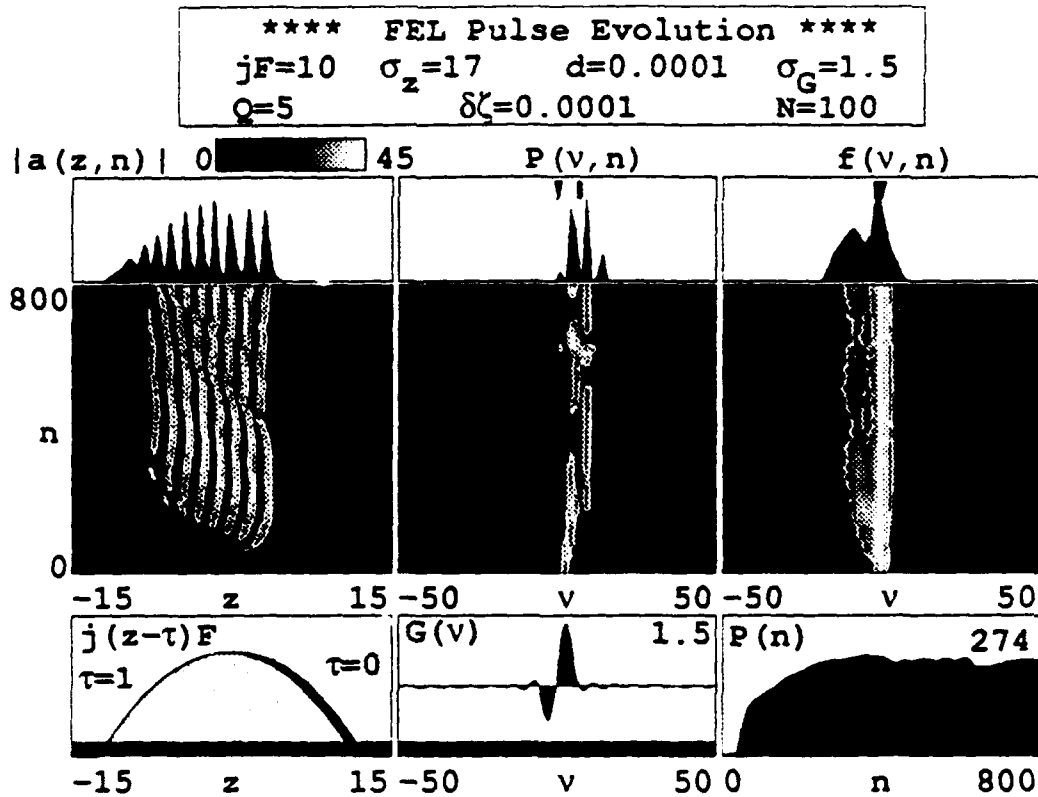indicates a very small change in the distance between mirrors

**** FEL Pulse Evolution ****
$jF=10$ $\sigma_z=17$ $d=0.0001$ $\sigma_G=1.5$
$Q=5$ $\delta\zeta=0.0001$ $N=100$

Figure 5-7.   APLE oscillator pulse evolution.

of $\Delta S \approx 0.1$ μm. A small random phase, $\delta\zeta=10^{-4}$, is added to each
of the electron phases to represent shot noise.   The shot
noise provides spontaneous emission for starting the FEL
oscillator.   The electron beam energy spread is $\sigma_G=1.5>1$ to
account for both exponential and Gaussian distributions.
However, when the oscillator saturates and the fields become
strong, the shape of the distribution is of little importance.
The factor $Q=5$ determines the resonator loss on each pass

through the undulator. The undulator consists of $N=100$ periods. The evolution of the optical field amplitude $|a(z,n)|$ (middle-left), shows unstable oscillation and the trapped-particle instability. The optical pulse length is ≈ 10 (FWHM) slippage distances. The window above shows the final optical field, where the modulation of the field envelope is clearly evident. The modulation is caused by the trapped-particle instability. The grey scale above $|a(z,n)|$ shows the peak field amplitude, $|a(z,n)| \approx 45$, in white, and zero field in black with one contour. Recall that $a_0 \approx 40\pi$ is required for one oscillation of trapped-particles. The power $P(n)$ increases as sidebands appear in the power spectrum, $P(v,n)$ (middle-center). The final power spectrum, $P(v)$ (top-center), has a significant sideband with optical power comparable to the fundamental. Again, the trapped-particle instability is evident. The pointed tick-mark at the top of the final power spectrum indicates the central wavelength of the initial radiation at resonance [12]. The rectangular tick-mark indicates the center of the final power spectrum. For reference, the weak-field gain spectrum, $G(v)$, is below the power spectrum on the same scale. It is calculated separately for $jF=10$ with no pulses [12]. The evolution of the electron's phase-velocity distribution after each pass, $f(v,n)$ (middle-right), indicates a relatively wide electron distribution with a narrow base. The final phase-velocity spectrum of the electrons in the beam, $f(v)$ is shown at the

top-right. The pointed tick-mark indicates the electron beam's initial phase-velocity at resonance. The position of the electron pulse, $j(z-\tau)F$ (lower-left), is indicated in dark grey at the beginning of the undulator, $\tau=0$, and is light grey at the end of the undulator, $\tau=1$. The unbunched electron pulse starts at $\tau=0$ and slips back to its position at $\tau=1$ on each pass, as bunching develops. The lower-right window shows the optical power, $P(n)$, after each pass. The optical power appears to reach steady state after $n\approx300$ passes. These observations correspond to the evolution of the optical field amplitude in the middle-left window.

Figure 5-8 shows the same oscillator as in Figure 5-7, but with a desynchronism of $d=0.01$. The electron spectrum is broader, this is especially evident after $\approx n=250$ passes when more electrons give up energy to the optical field. The optical pulse is longer, and forms coincidentally with the initial spread in the electron spectrum at $\approx n=50$ passes. The longer optical pulse is beneficial, because more of the electron pulse (lower-left) can interact with the optical field as the pulse slowly slips back from $\tau=0$ to $\tau=1$. This serves to increase the gain. The optical field evolution and the power evolution still show the trapped-particle instability. The oscillator exhibits relatively stable operation.

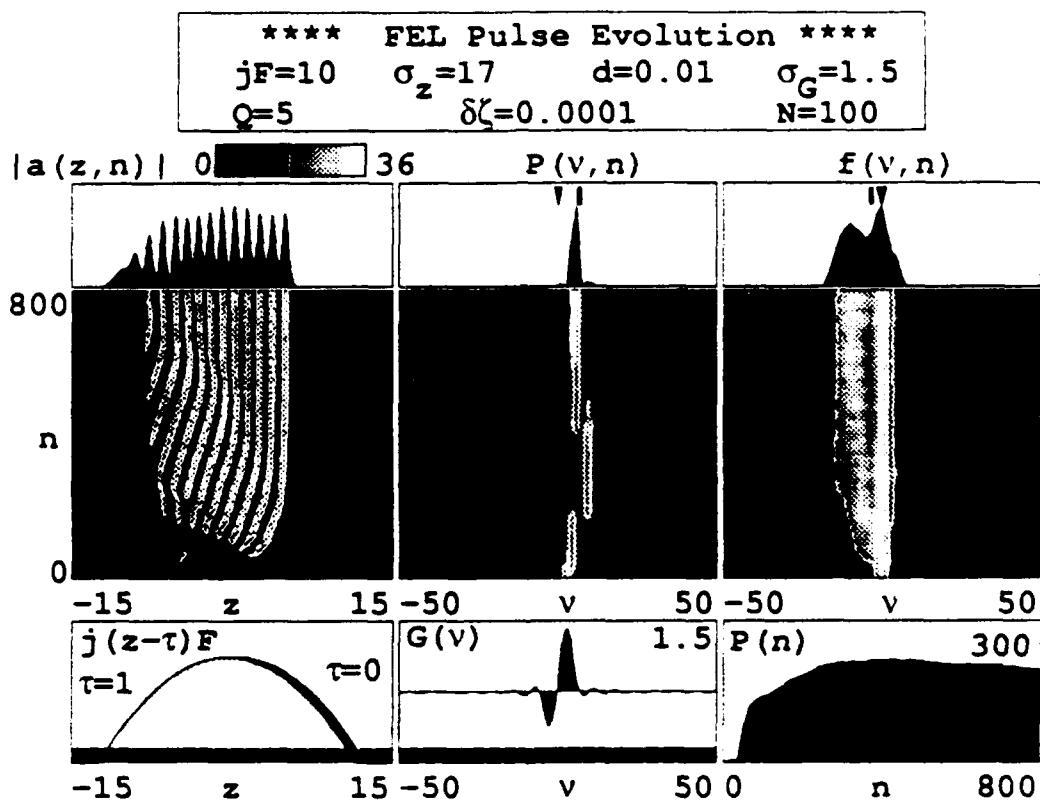Figure 5-9 shows the oscillator with a slightly larger desynchronism, $d=0.03$. Here, the electron spectrum is
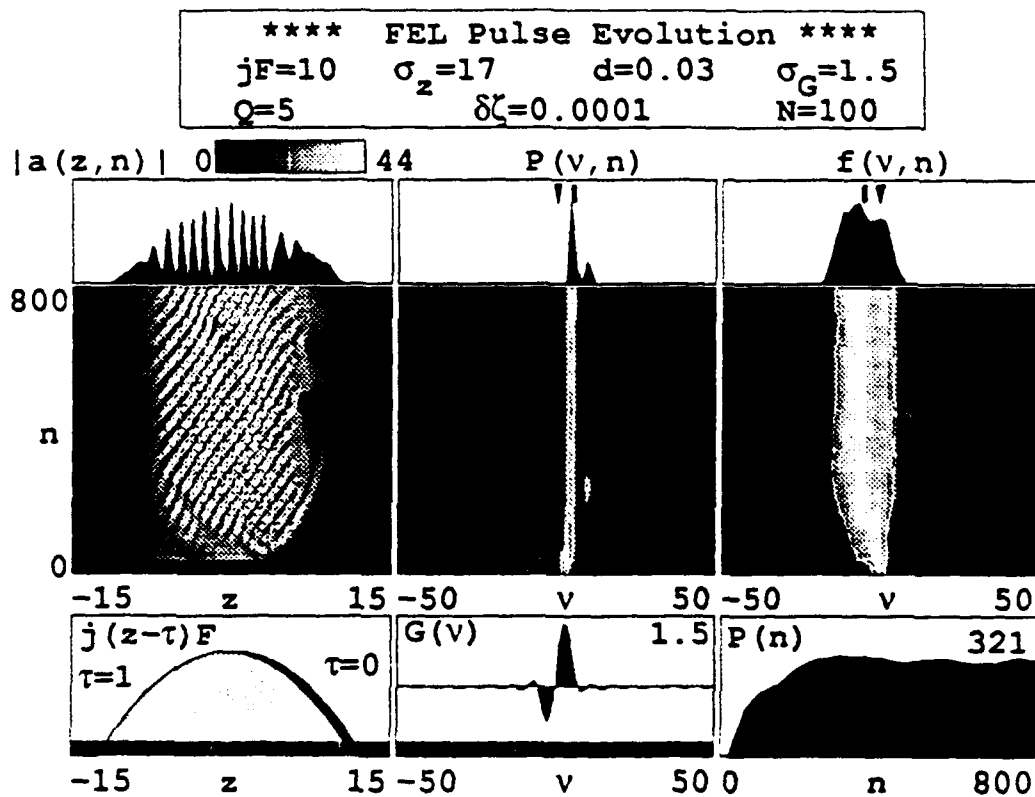
Figure 5-8. APLE oscillator with $d \approx 0.01$.

54

Figure 5-9. APLE oscillator with $d=0.03$.

broadest, extending further in the -v direction, indicating
that more electrons are giving up energy to the optical field.
The optical pulse is also longer, forming coincident with the
onset of the broad electron spectrum at $\approx n=100$ passes.   The
trapped-particle instability still exists.   The power may be
unstable because of chaotic optical modes.

Figure 5-10 shows the same oscillator with a still larger
desynchronism, $d=0.08$.   The broad electron distribution still
exists, although it is slightly narrower than that of the
previous figures.   The optical pulse length is about the same
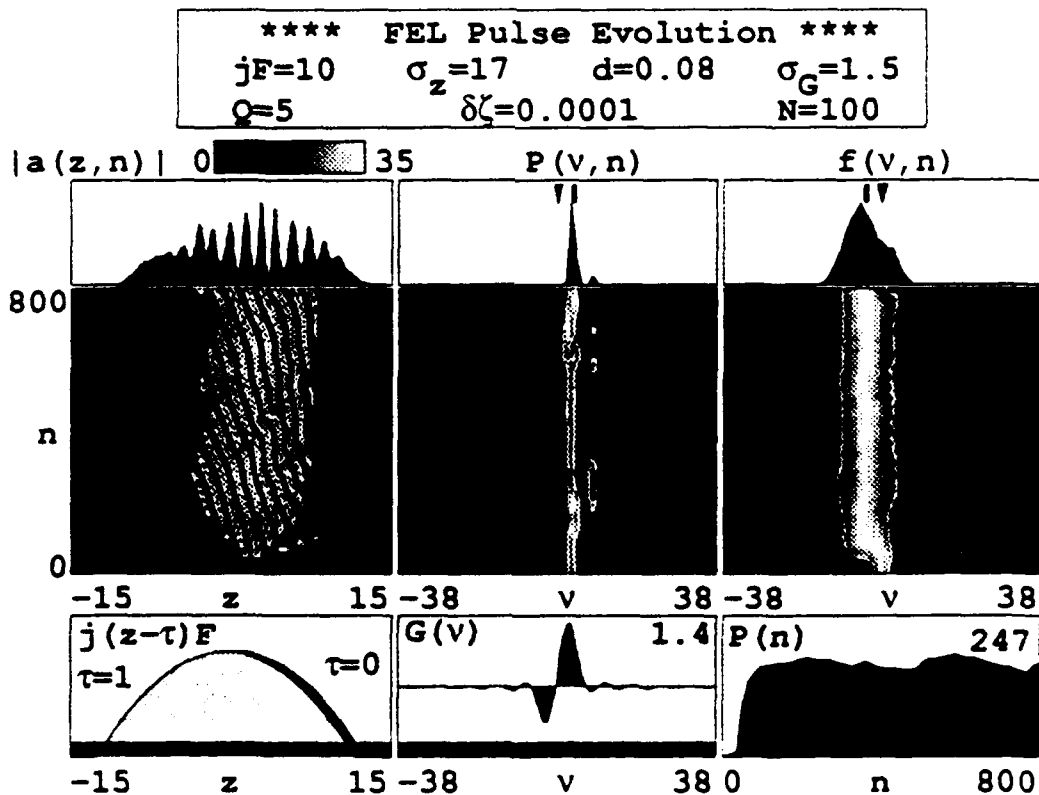as in Figure 5-9, but its amplitude has decreased.   Notice

Figure 5-10.   APLE oscillator with $d=0.08$.

that the power spectrum has a smaller sideband. The optical power is also less than that exhibited with $d=0.03$. However, the FEL operation appears to be stable.

Figure 5-11 shows the same oscillator as in Figure 5-10, but with a desynchronism $d=0.1$. The trapped-particle instability has decreased, as evidenced by the optical field evolution and the power evolution. The electron spectrum is slightly narrower than shown in Figure 5-10, and the optical pulse is shorter. These factors combine to cause a decrease in power.

We cannot explore larger values of desynchronism because of numerical limitations, but the trends indicated in the previous examples continue. As desynchronism increases further, the electron beam distribution is made smaller and the optical pulse is longer. Both of the effects are desirable for the amplifier performance.
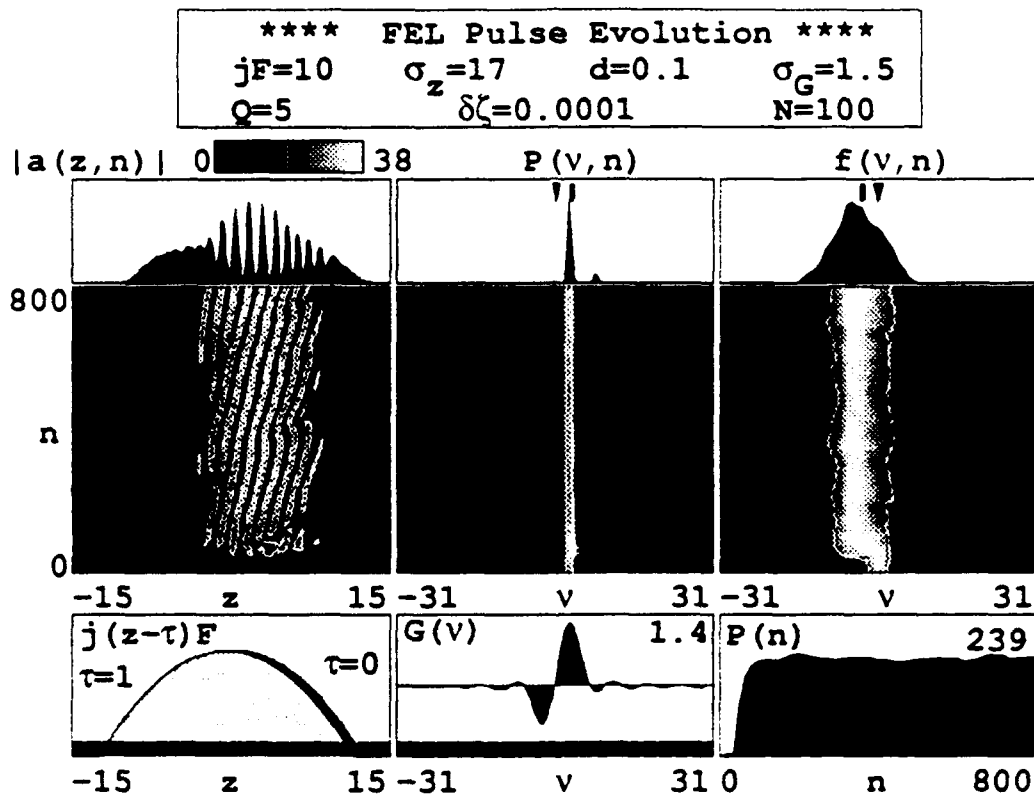
**** FEL Pulse Evolution ****

$jF=10$ $\sigma_z=17$ $d=0.1$ $\sigma_G=1.5$
$Q=5$ $\delta\zeta=0.0001$ $N=100$

$|a(z,n)|$ 0 ▮▮▮▮ 38 $P(\nu,n)$ $f(\nu,n)$

Figure 5-11. APLE oscillator with $d=0.1$.

58

VI.   THE APLE AMPLIFIER

A. DIFFRACTION EFFECTS

In this chapter, we use numerical simulations to investigate important features of the APLE amplifier. The method used to evaluate diffraction effects is similar to that used in the previous chapter. However, the pulse simulations evaluate a single-pass ($\tau=0{\to}1$) vice multiple passes, because the light and electrons traverse the amplifier only once. The evaluation of the amplifier is also different because it includes taper. With tapering included, the pendulum equation can be written as $\ddot{\zeta} = \delta\theta(|a|-a_s) + |a|\cos(\zeta+\phi)$ where optical field amplitude at saturation $a_s=2(j/2)^{2/3}$, θ is a step function, and δ represents taper [12].

The first step in this investigation is to follow the FEL wavefront evolution as τ goes from 0 to 1 along the $N=256$ period undulator, as illustrated in Figure 6-1. The dimensionless current density is $j=197000$, and the radius of the electron beam is $\sigma_e=0.09$. The initial optical field amplitude $a_0=18$. A gain spectrum simulation (similar to Figure 5-1) showed that peak gain is at $v_0\approx15$. The wavefront simulation is run at $v_0\approx15$ for peak gain in weak fields prior to saturation at field value $a_s=2(j/2)^{2/3}$. The beam quality is accounted for by using the distributions $\sigma_\theta=7$ and $\sigma_G=6$.

The dimensionless Rayleigh length $z_0=0.8$. The optical mode is focussed at the beginning of the undulator at $\tau_w=0$. The amount of taper is indicated by $\delta\approx-4\pi N K^2 \Delta K/K(1+K^2)\approx400\pi$.
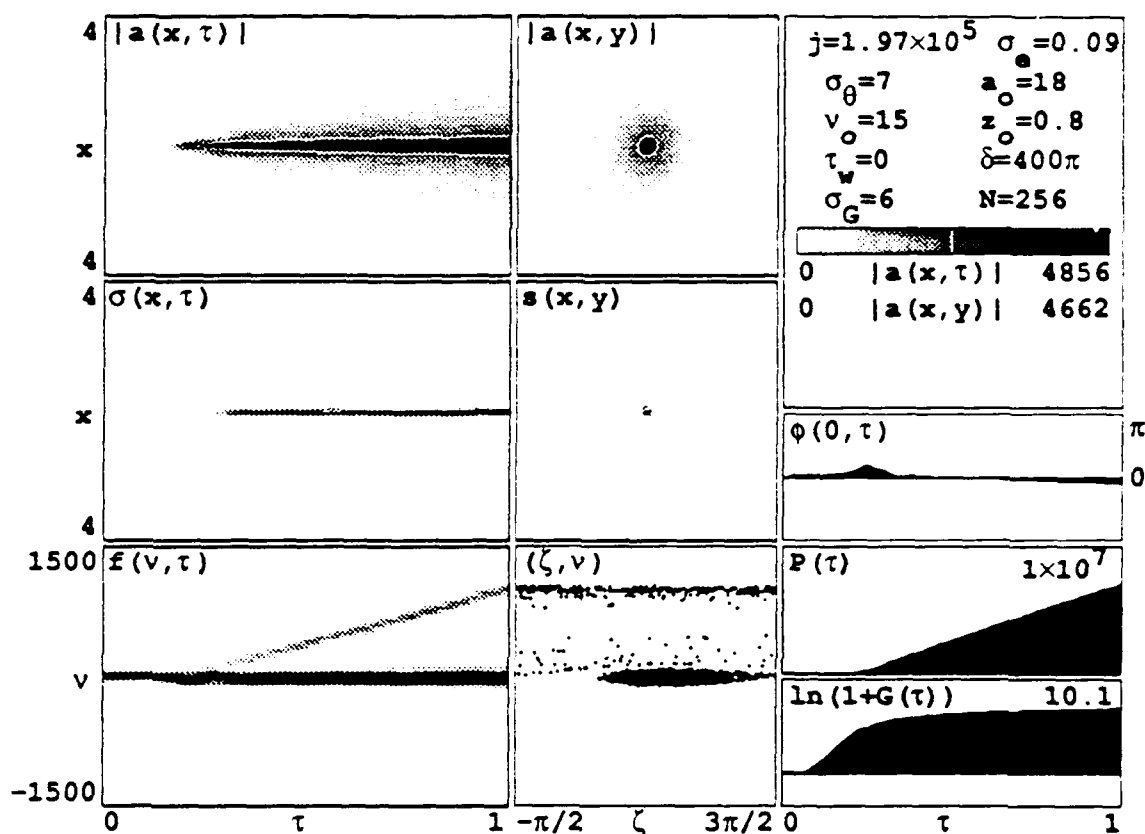

Figure 6-1. APLE amplifier wavefronts in strong fields.

The evolution of the optical mode amplitude, $|a(x,\tau)|$ (upper-left), shows that the peak field grows steadily through the undulator. Without focussing by the intense electron beam, the size of the optical mode at the end of the undulator would be $w=\sqrt{z_0}(1+1/z_0^2)^{1/2}\approx1.43$ where $z_0=0.8$. Instead, the optical mode radius is reduced to $w\approx0.3$. We obtain the filling factor by taking the ratio of the electron beam area,

60

$\sigma(x,y)$ (middle-center), to the optical mode area, $|a(x,y)|$ (upper-center). This ratio results in a filling factor $F \approx 0.10$. The focussing of the optical mode increases the value of F, and serves to increase the gain. The evolution of the bunching current, $\sigma(x,\tau)$ (middle-left), shows there is no bunching at the beginning of the undulator ($\tau=0$), but there is clear bunching at the end of the undulator ($\tau=1$). The electron phase-velocity distribution, $f(v,\tau)$ (lower-left), shows that about half the electrons become untrapped after $\tau > 0.25$ when the optical field reaches the saturation level $a_s \approx 2(j/2)^{2/3}$. Experience indicates that when in strong optical fields, the tapered FEL operates best when $\approx 50\%$ of the electrons remain trapped. Increasing the taper serves to untrap more electrons. The final electron phase-space distribution, (ζ,v) (lower-center), shows a large amount of electron bunching at the end of the undulator. Note that $\approx 50\%$ of the electrons are trapped. The spread in phase velocities due to the initial spread $\sigma_G \approx 6$ and $\sigma_\theta \approx 7$ is clearly visible. The plot of the optical field phase evolution at the center of the mode, $\phi(0,\tau)$ (on the right), indicates an increase in phase followed by a steady decrease. The power evolution, $P(\tau)$, shows a progressive increase in power as bunching develops. The gain, $G(\tau)$, also increases with the increased bunching of electrons; the final gain is $G_f \approx 25000$.

It can be shown that $\approx 10\%$ of the optical power, an average of ≈ 10 kW, strikes the inside surface of the beam pipe. Over

61

heating of the beam pipe may occur; therefore, this area should be investigated further.

B. PULSE EFFECTS

Figure 6-2 shows the optimum APLE amplifier pulse evolution over one pass with an initial field a_0=18, starting at v_0=15. The window width w=4 corresponds to four slippage distances along the beam, z is the longitudinal axis. The dimensionless current density is jF=20000, assuming $F \approx 0.10$. The dimensionless electron pulse length is σ_z=2 (FWHM). The undulator taper is $\delta \approx -4\pi N K^2 \Delta K/K(1+K^2) \approx 250\pi$, corresponding to
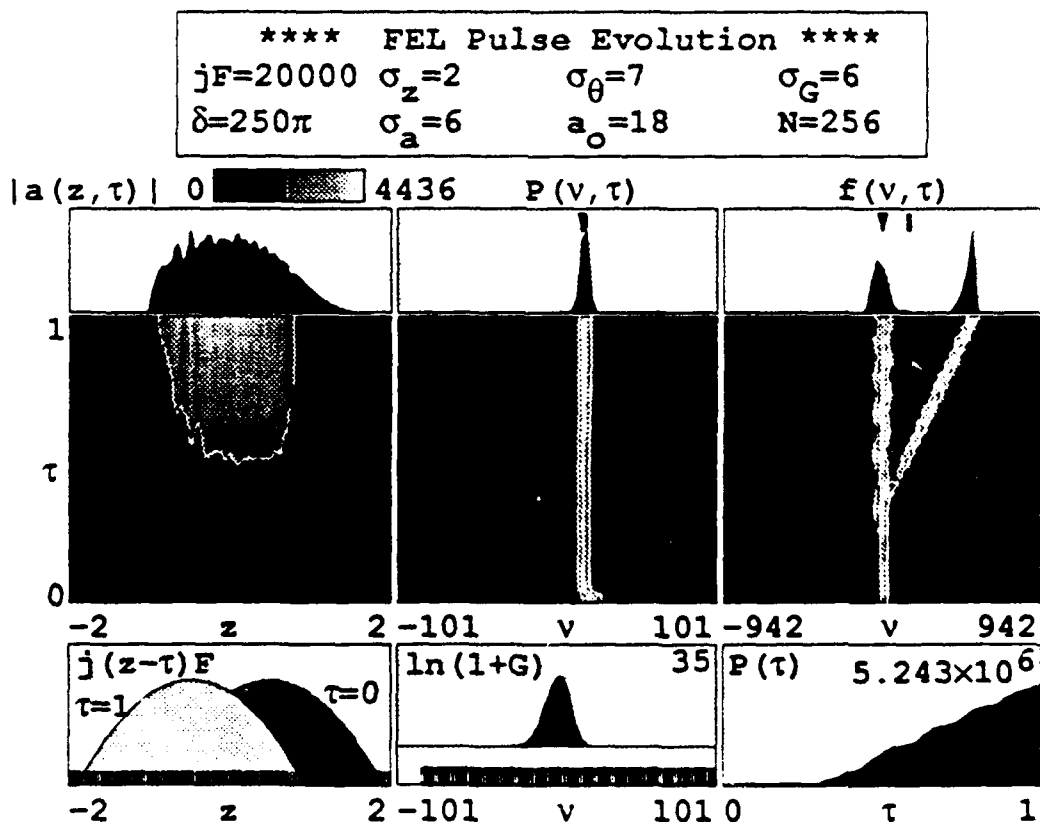

Figure 6-2. *APLE amplifier pulse evolution with σ_a=6.*

a taper of about 40% in the undulator field strength. The optical pulse width, $\sigma_a=6$ (FWHM), is found by taking the oscillator optical pulse length and normalizing it for the amplifier. The undulator consists of $N=256$ periods. The evolution of the electron's phase-velocity distribution, $f(v,\tau)$ (middle-right), must be viewed differently than in the case of the oscillator, since the amplifier is tapered (see Chapter III. F.). Recall that tapering maintains the optical field resonant with the electrons as they lose energy. Electrons trapped near resonance $v=0$ actually lose energy as they proceed through the undulator. The distribution shows electrons becoming untrapped about 40% of the way down the undulator when $|a|>a_s$. The trapped electrons, maintaining a phase velocity $v\approx0$ down the undulator, lose energy to the optical field thereby amplifying the light. The final phase-velocity spectrum of the electrons in the beam, $f(v)$, indicates that $\approx50\%$ of the electrons are trapped. The evolution of the optical field amplitude $|a(z,\tau)|$ (middle-left), shows growth coincident with the untrapping of electrons. The grey scale above $|a(z,n)|$ shows the peak field amplitude, $|a(z,\tau)|=4436$. The power spectrum, $P(v,\tau)$ (middle-center), is narrow. The final power spectrum, $P(v)$, has no sidebands; the trapped-particle instability is not present. Recall that the position of the electron pulse, $j(z-\tau)F$ (lower-left), is indicated in dark grey at the beginning of the undulator, $\tau=0$, and is light grey at the end

63

of the undulator, $\tau=1$. It is evident that there is significant optical field - electron pulse interaction. The lower-right window shows the optical power evolution through the undulator, $P(\tau)$. The optical power appears to grow steadily after electrons become untrapped at $\tau\approx0.4$. The efficiency $\eta\approx8.8\%$.

The use of a short optical pulse is an option being considered by researchers at Boeing. Therefore, we now investigate the amplifier's performance with a shorter optical pulse, now the same length as the electron pulse. Figure 6-3 shows the same amplifier as in Figure 6-2, but with an optical pulse $\sigma_a=2$. The electron spectrum indicates slight under trapping of electrons. Notice that the final power has decreased. The efficiency is also less, $\eta\approx7.6\%$.
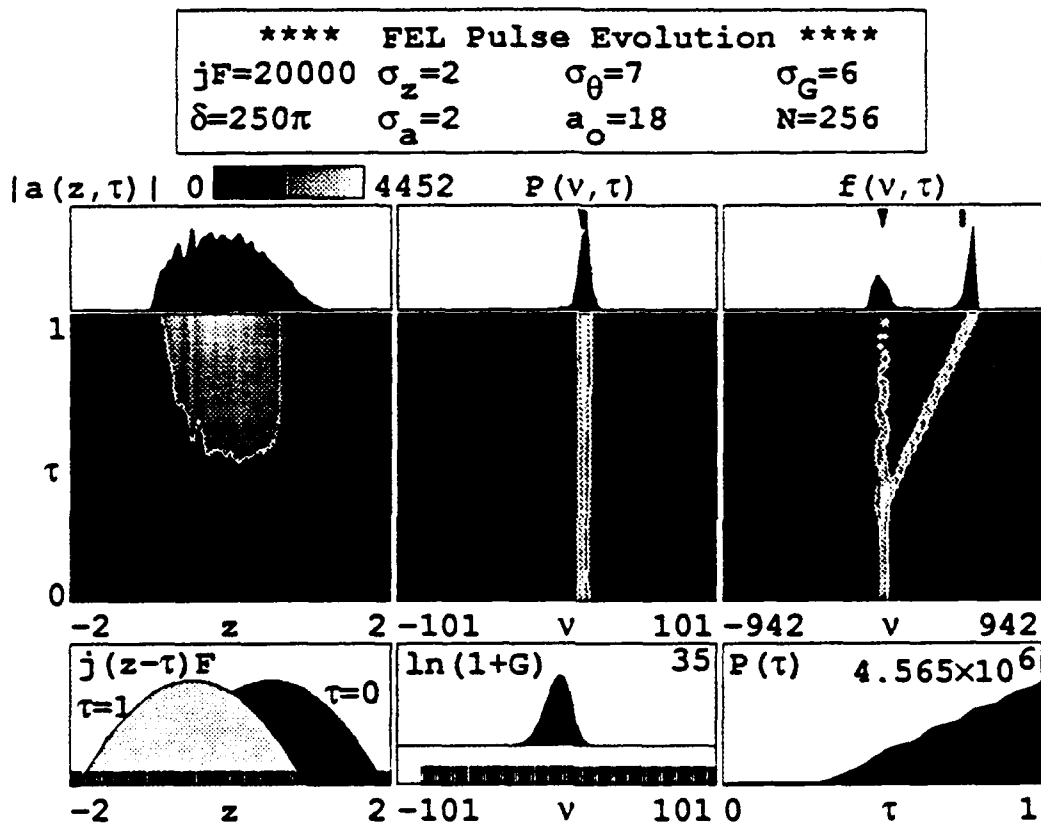
Figure 6-3. APLE amplifier pulse evoltion with $\sigma_a=2$.

VII. CONCLUSIONS

The demonstration of high average power is one of the important directions that FEL research is heading. When coupled with the FEL's demonstrated tunability and reliability, high average power will create a highly desirable directed energy system. The FEL's quick response time and "infinite magazine" also make it a candidate for military applications. Military applications include shipboard, land-based and airborne FELs. The advantages of directed energy and the FEL weapon specifically, were discussed herein. The FEL is likely the weapon of choice for the next century, and could have significant impact in many warfare areas, including Theater Ballistic Missile Defense (TBMD). The above features make the FEL attractive for scientific and industrial applications as well.

The proposed Boeing Average Power Laser Experiment (APLE) will demonstrate the highest FEL average power to date (100 kW); completion is scheduled for 1996. The APLE design appears feasible, and can result in successful attainment of the design goal.

The research addressed in Chapters V and VI provide some insight into the experiment. A relatively large desynchronism is beneficial to the oscillator. This results in stable performance and a long optical pulse. The long pulse, when

compared with a short pulse, optimizes the performance of the amplifier, resulting in both higher efficiency and higher power.

LIST OF REFERENCES

[1] J.M.J. Madey, "Stimulated Emission of Radiation in Periodically Deflected Electron Beams," *Journal of Applied Physics*, v. 42, 1971.

[2] Janne E. Nolan, and Albert D. Wheelon, "Third World Ballistic Missiles," *Scientific American*, v. 263 no. 2, August 1990.

[3] James Blackwell, *Thunder in the desert: the strategy and tactics of the Persian Gulf War*, Bantam Books, New York, 1991.

[4] U.S. News and World Report, *Triumph without victory: the unreported history of the Persian Gulf War*, Random House, New York, 1992.

[5] Michael Riezenman, "Revising the script after Patriot," *IEEE Spectrum*, September 1991.

[6] Stephan A. Fleet, *The Role of Air Operability in Tactical Missile Defense*, Air Command and Staff College, Maxwell AFB, Alabama, 1988.

[7] Interview between Ken W. Wallace, Lieutenant Commander, USN, Naval Postgraduate School, Monterey, California, and the author, 6 March 1992.

[8] R. Ernest Dupuy, and Trevor N. Dupuy, *The Encyclopedia of Military History from 3500 B.C. to the present*, Harper ard Row, New York, 1986.

[9] N Bloembergen, and others, "Report to the American Physical Society of the study group on science and technology of directed energy weapons," *Reviews of Modern Physics*, v. 59 no. 3 part II, July 1987.

[10] Carl A. Bice, *Theory for the CEBAF and Shipboard FELs*, Master's Thesis, Naval Postgraduate School, Monterey, California, December 1991.

[11] Kwang-Je Kim, and Andrew Sessler, "Free-Electron Lasers: Present Status and Future Prospects," *Science*, v. 250, 5 October 1990.

[12] William B. Colson, "Classical Free Electron Laser Theory," Chapter 5 in *Free Electron Laser Handbook*, W.B. Colson, C. Pellegrini and A. Renieri (eds.), North-Holland Physics, Elsevier Science Publishing Co., The Netherlands, 1990.

[13] J.B. Murphy,and C. Pellegrini, "Introduction to the Physics of the FEL," Chapter 2 in *Free Electron Laser Handbook*, W.B. Colson, C. Pellegrini and A. Renieri (eds.), North-Holland Physics, Elsevier Science Publishing Co., The Netherlands, 1990.

[14] Andrew M. Sessler, and Douglas Vaughan, "Free-Electron Lasers," *American Scientist*, v. 75, January 1987.

[15] J.D. Jackson, *Classical Electrodynamics*, John Wiley & Sons, New York, 1975.

[16] W.B. Colson, *Nuclear Instruments & Methods in Physics Research* A237, 1, 1985; W.B. Colson, Ph.D. Thesis, Stanford University, 1977.

[17] W.B. Colson, G. Dattoli, and F. Ciocci, *Physics Review* A31, 828, 1985.

[18] W.B. Colson, J.C. Gallardo, and P.M. Bosco, *Physics Review* A34, 4837, 1986.

[19] E.T. Scharlemann, "Single-Pass Free-Electron Laser Amplifiers," Chapter 9 in *Free Electron Laser Handbook*, W.B. Colson, C. Pellegrini and A. Renieri (eds.), North-Holland Physics, Elsevier Science Publishing Co., The Netherlands, 1990.

[20] J.C. Goldstein, and W.B. Colson, *International Conference on LASERS '81*, p. 93, ed. C.B. Collins, STS Press, 1981.

[21] G. Dattoli, A. Marino, and A. Renieri, *Physics of Quantum Electronics*, v. 8, 515, 1982.

[22] J.C. Goldstein, and W.B. Colson, *International Conference on LASERS '82*, p. 218, ed. R.C. Powell, STS Press, 1982.

[23] S. Benson, and J.M. Madey, *Free Electron Generators of Coherent Radiation*, C.A. Brau, S.F. Jacobs and M.O. Scully (eds.), SPIE 453, 55, 1983.

[24] M.N. Rosenbluth, H.V. Wong, and B.N. Moore, *Free Electron Generators of Coherent Radiation*, SPIE 453, 25, C.A. Brau, S.F. Jacobs and M.O. Scully (eds.), 1983.

[25] W.B. Colson, and A. Renieri, *Journal de Physique*, Colloque C1-44, 11, 1983.

[26] W.B. Colson, and Roger A. Freedman, *Optics Communication* 46, 37, 1983.

[27] Roger A. Freedman, and W.B. Colson, *Optics Communication* 52, 409, 1985.

[28] W.B. Colson, *Free Electron Generators of Coherent Radiation*, SPIE 453, 289, Brau, Jacobs, and Scully (eds.), 1984.

[29] D.C. Quimby, J.M. Slater, and J.P. Wilcoxon, *IEEE Journal of Quantum Electronics* QE-21, 979, 1985.

[30] N.M. Kroll, and M.N. Rosenbluth, *Physics of Quantum Electronics*, v. 7, 147, 1980.

[31] W.B. Colson, *Nuclear Instruments & Methods in Physics Research* A250, 68, North-Holland, Amsterdam, 1986.

[32] J.B. Romero, and others, "Boeing/Los Alamos average power free electron laser demonstration," to be published.

[33] D.C. Quimby, and D.J. Pistoresi, *Nuclear Instruments and Methods in Physics Research* Axxx, xx, North-Holland, Amsterdam, 1992.

[34] D. Shoffstall, private communication.

[35] D.H. Dowell, and others, *Nuclear Instruments and Methods in Physics Research* A304, 336, North-Holland, Amsterdam, 1991.

[36] D.H. Dowell, and others, *Nuclear Instruments and Methods in Physics Research* A304, 1, North-Holland, Amsterdam, 1991.

INITIAL DISTRIBUTION LIST

1. Defense Technical Information Center   2
    Cameron Station
    Alexandria, Virginia 22304-6145

2. Library, Code 52   2
    Naval Postgraduate School
    Monterey, California 93943-5000

3. Professor William B. Colson, Code PH/Cw   7
    Department of Physics
    Naval Postgraduate School
    Monterey, California 93943-5000

4. Professor John R. Neighbours, Code PH/Nb   1
    Department of Physics
    Naval Postgraduate School
    Monterey, California 93943-5000

5. Professor K. E. Woehler, Code PH/Wh   1
    Department of Physics
    Naval Postgraduate School
    Monterey, California 93943-5000

6. Captain R. M. Cassidy   1
    Aegis Program Office
    James Polk Building
    2521 Jefferson Davis Dr.
    NC 2 10th Floor
    Arlington, Virginia 22202

7. Dr. David Merrit   1
    SPAWAR 23
    Space and Naval Warfare Systems Command
    Rm 309, 5 Crystal Park
    2451 Crystal Drive
    Arlington, Virginia 22202